DOE F 2050.11
(2-87)
(Previous GC-792)

OMB Control No.
1910-0800

PATENT CERTIFICATION

University of South Dakota
Contractor

☐ Interim Certification
☑ Final Certification

DE-FG02-08ER64624
DOE Prime and/or Subcontract Nos.

Contractor hereby certifies that:

1. All procedures for identifying and disclosing subject inventions as required by the patent clause of the contract have been followed throughout the reporting period.

2. There were no subcontracts or purchase orders involving research, development, and demonstration except as follows: [State none when applicable.]
South Dakota School of Mines and Technology (Subaward USD-08-03) USD1210

3. No inventions or discoveries were made or conceived in the course of or under this contract other than the following *(Certification includes ☑, does not include ☐ all subordinates):*

[State none when applicable.]

TITLE	INVENTOR	DATE REPORTED	DOE "S" NO.*
none			

4. The completion date of this contract is as follows:

5. The following period is covered by this certification:

January 11 2011 to March 31 2014
Month Day Year Month Day Year

University of South Dakota
Contractor

414 E. Clark St.
Vermillion, SD 57069
Address

Signature

James Hoefelmeyer

10.3.14
Date of Certification

* Also include Subcontract No. If available

FEDERAL FINANCIAL REPORT

(Follow form instructions)

1. Federal Agency and Organizational Element to Which Report is Submitted	2. Federal Grant or Other Identifying Number Assigned by Federal Agency (To report multiple grants, use FFR Attachment)	Page	of
Nat Institute of Dental & Craniofacial Research	DOE DE-FC02-08ER64624	1	1 pages

3. Recipient Organization (Name and complete address including Zip code)
University of South Dakota
105 Slagle Hall 414 E. Clark St.
Vermillion, SD 57069

4a. DUNS Number	4b. EIN	5. Recipient Account Number or Identifying Number (To report multiple grants, use FFR Attachment)	6. Report Type	7. Basis of Accounting
929930808	466003541	240068	Quarterly ☐ Semi-Annual Annual X Final	Cash

8. Project/Grant Period From: (Month, Day, Year)	To: (Month, Day, Year)	9. Reporting Period End Date (Month, Day, Year)
8/1/2008	3/31/2014	3/31/2014

10. Transactions	Cumulative
(Use lines a-c for single or multiple grant reporting)	
Federal Cash (To report multiple grants, also use FFR Attachment):	
a. Cash Receipts	$2,121,200.00
b. Cash Disbursements	$2,121,200.00
c. Cash on Hand (line a minus b)	$0.00
(Use lines d-o for single grant reporting)	
Federal Expenditures and Unobligated Balance:	
d. Total Federal funds authorized	$2,121,200.00
e. Federal share of expenditures	$2,121,200.00
f. Federal share of unliquidated obligations	$0.00
g. Total Federal share (sum of lines e and f)	$2,121,200.00
h. Unobligated balance of Federal funds (line d minus g)	$0.00
Recipient Share:	
i. Total recipient share required	$0.00
j. Recipient share of expenditures	$0.00
k. Remaining recipient share to be provided (line i minus j)	$0.00
Program Income:	
l. Total Federal program income earned	$0.00
m. Program income expended in accordance with the deduction alternative	$0.00
n. Program income expended in accordance with the addition alternative	$0.00
o. Unexpended program income (line l minus line m or line n)	$0.00

11. Indirect Expense	a. Type	b. Rate	c. Period From	Period To	d. Base	e. Amount Charged	f. Federal Share
		43.5%	7/1/2011	3/31/2014	821011.49	357140	357,140.00
				g. Totals:			357,140.00

12. *Remarks: Attach any explanations deemed necessary or information required by Federal sponsoring agency in compliance with governing legislation:*

13. **Certification: By signing this report, I certify that it is true, complete, and accurate to the best of my knowledge. I am aware that any false, fictitious, or fraudulent information may subject me to criminal, civil, or administrative penalties.** (U.S. Code, Title 218, Section 1001)

a. Typed or Printed Name and Title of Authorized Certifying Official	c. Telephone (Area code, number and extension)
Jerald R. Bartling Grants Administrator	605 677 6848
	d. Email address Jerry.Bartling@usd.edu
b. Signature of Authorized Certifying Official	e. Date Report Submitted (Month, Day, Year) 9/30/2014
	14. Agency use only:

Standard Form 425
OMB Approval Number: 0348-0061
Expiration Date: 10/31/2011

Paperwork Burden Statement
According to the Paperwork Reduction Act, as amended, no persons are required to respond to a collection of information unless it displays a valid OMB Control Number. The valid OMB control number for this information collection is 0348-0061. Public reporting burden for this collection of information is estimated to average 1.5 hours per response, including time for reviewing instructions, searching existing data sources, gathering and maintaining the data needed, and completing and reviewing the collection of information. Send comments regarding the burden estimate or any other aspect of this collection of information, including suggestions for reducing this burden, to the Office of Management and Budget, Paperwork Reduction Project (0348-0061), Washington, DC 20503.

U.S. DEPARTMENT OF ENERGY JUNE 2005

FINANCIAL ASSISTANCE
PROPERTY CLOSEOUT CERTIFICATION

Award Number	Recipient *(Name and address)*
DE-FG02-08ER64624	University of South Dakota 414 E. Clark St. Vermillion, SD 57069

The purpose of this report is to facilitate the closeout of the Award. Based on the records maintained by the Recipient in accordance with the Property Management standards set forth in the Award, the following data reflects the Recipient's closeout inventory of real and personal property that was provided by the Department of Energy (DOE) or partially or wholly acquired with project funds.

I. EQUIPMENT

A. **Federally-Owned**: *(Government Furnished Equipment): (10 CFR 600.133(a), 600.232, 600.322, or Federal Demonstration Partnership (FDP) General Terms and Conditions No. 33, as applicable):* ☒ No ☐ Yes

*(If **yes,** attach property inventory list that includes item description, manufacturer, model, serial number, original acquisition date, original acquisition cost and disposal condition code per the Federal Management Regulation 102-36.240)*

B. **Equipment Acquired with Award Funds where Title Vests in the Recipient with further obligations to DOE:**
(10 CFR 600.133, 600.134, 600.232, or 600.321, as applicable)

☒ No ☐ Yes

If **yes,** does the equipment have a per unit fair market value of $5,000 or more? ☐ No ☐ Yes

*(If **yes**, attach a property inventory list that includes item description, manufacturer, model, serial number, original acquisition date, original acquisition cost, disposal condition code per the Federal Management Regulation 102-36-240 and one of the disposition codes listed below)*

(1) The property will continue to be used for the purposes authorized in the Award.

(2) The property is no longer needed for the purposes of the Award, and will be used on another Federally sponsored activity *(List Activity and Federal Agency):*

(3) The Recipient wishes to retain the property and compensate DOE for its share of the current per unit fair market value. *(Identify the fair market value on the attached property inventory list and describe how the value was determined).*

(4) The property is no longer needed for the purposes of the Award or other Federally sponsored activities and the Recipient requests DOE disposition instructions.

II. SUPPLIES *(10 CFR 600.135, 600.233, 600.324, or FDP General Terms and Conditions No. 35, as applicable)*

Does the residual inventory of unused supplies exceed $5,000 in total aggregate value? ☒ No ☐ Yes *(if **yes**, check block below)*

☐ The supplies will be used on another Federally sponsored activity *(List Activity and Federal Agency).*

☐ The supplies will be sold or retained for use on non-Federally sponsored activities and the Recipient will compensate DOE for its share of the sales proceeds (or estimate of current fair market value). Attach a list of the supplies and complete the following Worksheet:

Sale proceeds or estimate of current fair market value	$_____
Percentage of Federal participation	_____%
Federal share	$_____
Selling and handling allowance	$_____
Amount to be remitted to DOE	$_____

U.S. DEPARTMENT OF ENERGY

FINANCIAL ASSISTANCE
PROPERTY CLOSEOUT CERTIFICATION

III. REAL PROPERTY: *(Real Estate - 10 CFR 600.132, /600.231, 600.321, or FDP General Terms and Conditions No. 32, as applicable)* ☒ No ☐ Yes *(If **yes,** complete A –C)*

A. Description of Real Property:

B. Complete Address of Real Property:

C. Period of Federal Interest in the Property: From _____ To _____ (Unless the award specifies otherwise, the Federal Interest in the property ends when the award project period ends.)

D. Disposition Preference Request. If the period of Federal Interest in the property exceeds the project period, check one of the following blocks to indicate your disposition preference:

- ☐ Transfer property to another Federal award.
- ☐ Sell and compensate DOE.
- ☐ Return to DOE.
- ☐ Retain title and compensate DOE for its share of the current fair market value of the property.

Certification: I certify to the best of my knowledge and belief that all information presented in this report is true, correct and complete, and constitutes a material representation of fact upon which the Federal government may rely.

Name	Signature	Title	Date
James Hoefelmeyer		Associate Professor of Chemistry (PI)	10.3.14

FINANCIAL ASSISTANCE
PROPERTY CLOSEOUT CERTIFICATION

To be completed by the Department of Energy:

DOE PROPERTY DISPOSITION

☐ **Negative Report**

☐ **Real Property:**

☐ **Equipment:**

☐ **Supplies:**

Property Management Official Name	**Signature**	**Date**

Final technical report for contract DE-FG02-08ER64624

Institution: University of South Dakota

PI: James Hoefelmeyer

Reporting period: 1/1/2011-3/31/2014

Introduction

The purpose of the project was to establish a catalysis research group in South Dakota, to build the capacity and capabilities of this group due to limited available research infrastructure in South Dakota, and to investigate key challenges in solar energy utilization and hydrogen fuel cells.

The project was initiated in 2008 and was funded in two parts of ca $1M each. The first award was issued in 2008 and concluded in 2010. The second award was approved for 2011; however due to budget sequestration, the funds did not arrive until the end of 2011 (nearly one full year into the project period). For this reason, a no-cost extension was requested and granted with final project date of 3/31/2014.

Project Objectives

The proposal objectives are divided into two components: infrastructure building and science.

Infrastructure building:
1. Develop a research cluster that addresses the following:
a. Research in a scientific field relevant to DOE
b. Multidisciplinary research cluster
c. Builds on existing state resources
d. Competitiveness and sustainability
e. Address a significant technological challenge
f. Potential for technology development and commercialization
2. Purchase key pieces of instrumentation to enable competitive research
3. Establish significant collaborations with DOE National Laboratories
4. Increase outside visibility of South Dakota research

Science:
Solar energy utilization requires conversion between forms of energy. Conversion of light energy to chemical energy using photocatalysis and chemical energy to electrical energy in fuel cells in tandem allows execution of a closed chemical cycle that captures solar energy and delivers electrical energy for work. We pursued several strategies to develop new photocatalyst materials and fuel cell catalyst and support materials.

1. Photocatalysts for solar water splitting
a. synthesis of nanocrystal components
b. immobilization of hybrid nanocrystals in membranes
c. characterization of nanocomposite material with sum-frequency generation spectroscopy
d. utilize ceramic capillaries as support of nanocomposite membranes
2. Electrospun carbon nanofelts as supports for improving performance of fuel cells
a. Preparation and Characterization of the Electrospun Carbon Nanofelt Made from PAN and/or PVA Nanofiber Nanofelt Precursors
b. Fabrication and Evaluation of the Prototype Fuel Cells Made of the Electrospun Carbon Nanofelt, Investigation on Durability (in-situ Oxidation/Degradation) of the Prototype Fuel Cells

Results

Infrastructure building:

1. A research cluster (named South Dakota Catalysis Group, or SDCG) consisting of eight investigators from two SD institutions (U. South Dakota and SD School of Mines & Technology) was formed. The cluster included faculty members from chemistry, chemical engineering, and nanoscience with expertise in materials synthesis and (photo)catalysis.

1a. The South Dakota Catalysis Group (SDCG) conducts research on advanced catalytic materials for solar energy utilization, specifically, hydrogen production and hydrogen fuel cells. The long-term vision of this project is to enable solar energy utilization on large scales in a process that is economically attractive. Requisite to this goal are photocatalyst materials for high-efficiency solar-to-chemical energy conversion, materials for robust fuel cell catalysis, and industrial engineering that produces devices through hierarchical assembly of nanostructures in a rapid and low-cost process. The principle foci of the current SDCG efforts are: 1) the development, through the application of nanotechnology, of a reactor in which a photocatalyst uses sunlight to split water to hydrogen and oxygen, and 2) development of improved supports and catalysts for fuel cells. The two foci represent complimentary approaches to solar energy utilization. The end products of the two research thrusts, photocatalyst and fuel cell, when used in conjunction, allow production of electricity from sunlight, storage of solar energy as chemical fuel, and zero net consumption of resources or production of atmospheric emissions. The research of SDCG is closely related to the DOE mission, in particular, Basic Research Needs in Solar Energy Utilization and Basic Research Needs in Catalysis for Energy.

1b. The SDCG included faculty with backgrounds in physical chemistry, inorganic chemistry, materials, (photo)catalysis, chemical engineering, polymers, organic chemistry, and ceramics.

1c. The SDCG was envisioned at a time when state investments in research infrastructure were rising. The Rounds administration in SD supported formation of several Governor's 2010 Research Centers, and was active in supporting SD EPSCOR efforts to build infrastructure. The state also newly implemented PhD programs in Materials Chemistry at U. South Dakota and Nanoscience at SD School of Mines & Technology. Thus the SDCG could interact synergistically with the active research investments at the state and federal level.

1d. In order that the SDCG become a sustainable research entity, it would have to build research competitiveness and develop a funding strategy.

The SDCG used the DOE investment to support projects that have gained significant traction. SDCG investigators have become increasingly successful in publication of high impact research (over 50 publications from the group) and attracting external funding. The synergy between SDCG activities and other research activities in the state of South Dakota was surely instrumental in sustaining a high level of growth in research productivity in SD institutions. In particular, South Dakota was awarded an NSF RII Track 2 award (Photo-active Nanoscale Systems) and an NSF IGERT award. SDCG investigators have been active contributors in those projects in addition to DOE funded activities.

1e. SDCG research addressed DOE Basic Research Needs as outlined in Basic Research Needs in Solar Energy Utilization and Basic Research Needs in Catalysis for Energy documents that address significant technological challenges.

1f. SDCG research has potential for technology development and commercialization.

2. SDCG has acquired several pieces of instrumentation to increase research capacity, including: gas-chromatograph, fuel cell test station, high temperature graphitization furnace, Langmuir-Blodgett trough, zetasizer, microbalance, total organic carbon analyzer, gas sorption analysis, and photochemical reactors.

3. Several SDCG investigators have actively collaborated with DOE laboratories. The relationships include user proposals at ORNL-CNMS, LBL-NCEM, and ANL.

4. SDCG investigators (and their work) are gaining attention. It was a key goal to move the visibility of research outside state borders. Part of the strategy was to develop collaborations outside of the state, including national labs. Investigators have been active participants at national meetings of the American Chemical Society and Materials Research Society and are publishing in leading journals.

Science:

1. Photocatalysts for solar water splitting.

New nanostructured photocatalyst materials have been developed that have ability to absorb visible light, separate electrons/holes, and utilize charge-carriers on separate catalytic sites. A method was devised to adsorb earth-abundant transition metal ions on the surface of semiconductor nanocrystals that could lead to numerous combinations of new nanostructured materials with potential application in photocatalysis.

1a. synthesis of nanocrystal components

Facile Method to Attach Transition Metal Ions to the Surface of Anatase TiO2 Nanorods

A robust, low-cost method to attach transition metal ions directly to the surface of anatase TiO2 rod-shaped nanocrystals with preservation of the host nanocrystal morphology and phase was developed. The procedure has been optimized to achieve quantitative control of metal ion loading on the surface of the nanorods. The metal ion can be attached to the nanocrystal surface up to full monolayer coverage, after which the surface becomes saturated and there is no further addition.

TiO2 nanorods were synthesized in gram-scale quantities according to the procedure reported by Hyeon.[14] The oleic acid stabilized anatase TiO2 nanorods dispersed readily in non-polar solvents and were characterized with powder X-ray diffraction (XRD), transmission electron microscopy (TEM), and UV-visible spectroscopy (Figure 1). Powder XRD of the sample shows broadened diffraction peaks, typical of nanocrystals, with reflections at 25.3°, 38.1°, 48.1°, 54.6°, 63.0°, 69.3°, and 75.4° (2θ) that correspond to d-spacings of 0.350 nm, 0.236 nm, 0.188 nm, 0.169 nm, 0.148 nm, 0.135, and 0.125 nm, respectively. The peak at 25.3°(2θ) corresponds to the (101) plane of anatase TiO2 (JCPDS file 21-1272). The (004) reflection at 38.1 (2θ) shows high relative intensity and narrow linewidth, and is evidence of elongation of the nanocrystal along the c-axis. TEM shows the presence of rod-shaped nanocrystals (diameter = 3.3 ± 0.4 nm; length = 43.3 ± 7.6 nm). At higher magnification, lattice fringes with separation of 0.35 nm were readily apparent that arise from the {101} lattice planes (d-spacing = 0.351 nm; JCPDS file 21-1272). Nanocrystals viewed through [100] show intersection of lattice fringes from (011) and (01-1) planes at an angle of 43°, in agreement with theory. The fast Fourier-transform also revealed less prominent lattice fringes associated with the (004) planes.

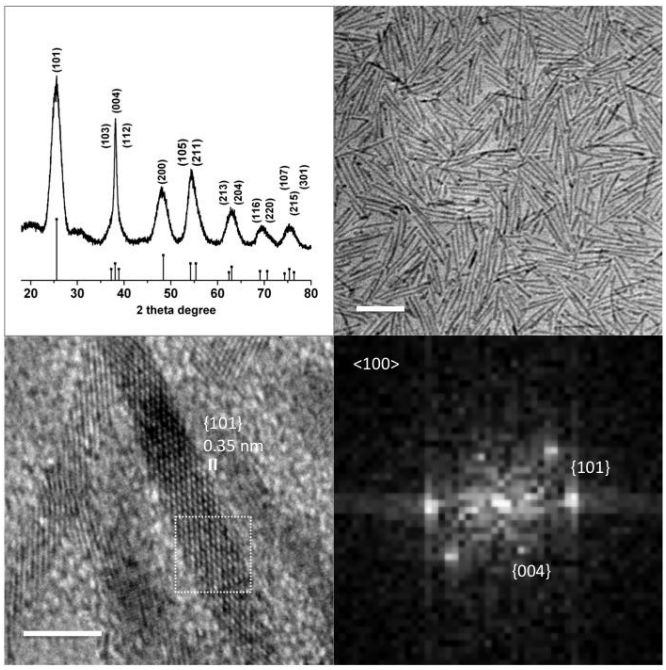

Figure 1. TiO2 nanorods were characterized with powder X-ray diffraction (top left; JCPDS file 21-1272 for anatase shown for comparison) and transmission electron microscopy. The scale bar = 50 nm (top right) and 5 nm (lower left). An FFT of the boxed region in the high-resolution image is shown (lower right).

A brief description of the experimental procedure for metalation of TiO2 nanorods is as follows. A flask was charged with a dispersion of TiO2 nanorods in hexanes, oleylamine, and octadecene, heated to 120°C under vacuum to drive off volatiles, and then cooled to room temperature. Under flow of N2, the desired metal chloride hydrate was added. The contents were heated at an optimized temperature, dependent on the metal, for 3 hours. Shorter reaction times or lower-than-optimum temperatures led to less efficient metal loading; whereas, longer reaction times or higher-than-optimum temperatures led to precipitation of nanocrystal aggregates or bulk metal precipitate. The nanorods were recovered after five cycles of precipitation with isopropanol, centrifugation, and redispersal in hexanes, in order to ensure complete removal of any unbound metal ions. The synthesis was reproducibly demonstrated for Mn+ = Cr(III), Mn(II), Fe(II), Co(II), Ni(II), and Cu(II). Dispersions of metalated nanorods have colors that are characteristic of the metal-ion; UV-vis absorbance spectra of the M^{n+}-TiO2 nanorods are shown in Figure 2. Powder X-ray diffraction and TEM data of the samples before and after the metalation procedure are identical, indicating retention of the nanorod morphology and crystal phase with no additional metal or metal oxide phases.

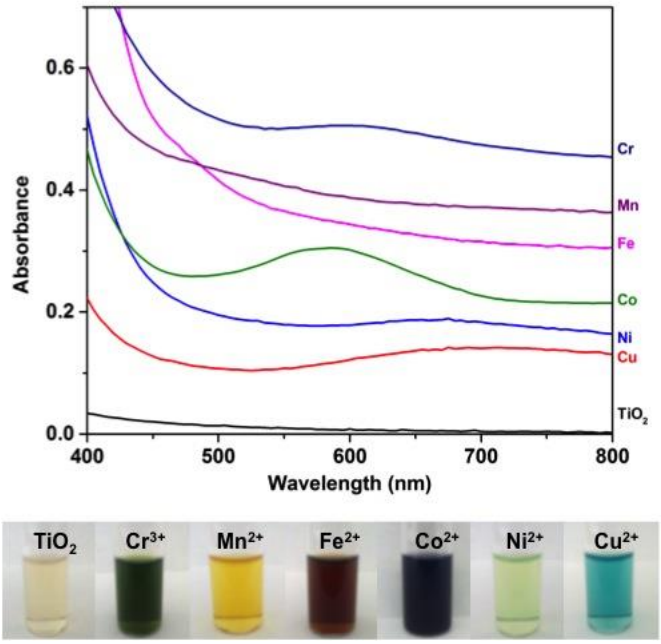

Figure 2. UV-vis spectra (stacked with offset of 0.07 a.u.) and photographs of metalated TiO2 NR dispersions in hexane.

The attachment of Mn+ onto the TiO2 nanorod surface is significantly influenced by the ratio of oleylamine:metal. The metal chloride hydrate precursors are completely insoluble in octadecene and the oleylamine solubilizes the metal salts. In solution, the metals can adsorb onto the surface of the TiO2 nanocrystal. We show vide infra that the adsorption behaviour follows the Langmuir adsorption model for a type I chemisorption isotherm. At equilibrium, the rate of adsorption is equal to the rate of desorption, and the equilibrium constant is equal to the ratio of the adsorption:desorption rate constants. Both processes are dependent on oleylamine; in the former it leads to elevated concentration of adsorbate in solution and in the latter it can compete with surface Ti-O groups to coordinate the transition metal ions. To determine the optimum oleylamine:metal conditions in which adsorption efficiency is highest, we performed a series of experiments altering the concentration of oleylamine while keeping a constant mole ratio of M:TiO2 well below surface saturation coverage (see section 1.3 in SI). Elemental analysis of each sample revealed the actual M:TiO2 ratio. Optimum conditions were found for all of the metal ions, presumably at which the metals were effectively solubilised while the equilibrium between metal ion in solution and the nanorod surface was not shifted too far toward the former. However, we expect the rate constants for adsorption and desorption to be dependent on the transition metal ion adsorbate. Therefore, the equilibrium constant for the adsorption reaction is dependent on the transition metal ion adsorbate. It is probable that this is partially manifest in the temperature dependence for adsorption of the transition metal ions onto the surface of the TiO2 nanocrystals.

Using the optimized synthesis procedure, we set out to demonstrate the adsorption behaviour of the transition metal ions on the surface of TiO2 nanocrystals. The M:TiO2 mole ratio was adjusted from 0.01-1 and the nanorods recovered from each synthesis (after five cycles of precipitation and redispersion to remove unbound ligands and metals) were characterized using elemental analysis (Figure 3). In particular, the cobalt system could be evaluated conveniently with UV-vis spectroscopy in addition to elemental analyses. A plot of absorbance (590 nm) versus theoretical Co:TiO2 mole ratio (based on moles Co added to moles TiO2) shows linear increase up to ~0.1 after which the slope becomes zero indicating saturation of the surface sites on the TiO2 with Co(II) (figure 3). We note that reactions with Co:TiO2 above this limit give blue colored supernatant upon precipitation of the nanorods with isopropanol, whereas, the supernatant is nearly colorless below the saturation limit. Elemental analysis of the recovered Co(II)-TiO2 nanorods shows an identical trend to the UV-vis spectroscopic data. The data indicate the adsorption of the metal ions to the surface of TiO2 nanocrystals exhibits type I Langmuir adsorption kinetics. At the saturation limit, the average mass fraction of cobalt in calcined samples was 0.118 (standard deviation = 0.011), corresponding to a Co:TiO2 mole ratio of 0.181 (standard deviation = 0.018). Based on geometric considerations, the surface site density for coordination of Co(II) to the surface of TiO2 can be estimated (see section 1.6 in SI). The ratio of surface:total Ti atoms, D, is 0.44. Based on the {101} surface, there are four Ti per unit plane. Two of the Ti in this unit plane are 5-coordinate Ti (Ti5c) terminated by hydroxo groups in an aqueous environment. Petsi et al found the most probable surface bonding mode for the TiO2 surface and Co(II) is a TiO-TiO bidentate geometry.[8a] Based on this finding, the theoretical ratio of Co:Ti for a saturated surface is D/2 = 0.22, which is in close agreement to our finding of Co:Ti = 0.18 in saturated samples. We also note that the surface density of the Ti5c sites is 5.18/nm2, which is consistent with the D/2 calculation.[16] The UV-vis absorbance and elemental analysis data demonstrate that we can effectively titrate the surface sites of the TiO2 nanorods. Powder X-ray diffraction and TEM data establish that the integrity of the TiO2 nanocrystal is not compromised and that no other crystal phases are formed, even when the surface is saturated with Co(II) (Figure S16). The Langmuir adsorption behaviour was observed for all of the metal ions with retention of the TiO2 nanocrystal phase and morphology. We never observe the mole ratio M:Ti > 0.22. Two metal ions (Fe2+ and Co2+) closely approach this limit; whereas, Ni2+ and Cu2+ are well below this limit. This is most likely due to the weaker adsorption of those metal ions to the TiO2 surface within the window of conditions in which adsorption occurs, and we note that Ni2+ and Cu2+ tend to prefer coordination to nitrogen bases rather than oxygen bases due to their larger ionic radii. Despite this limitation, we show a highly versatile, facile, inexpensive route to add transition metal ions to the surface of TiO2 nanocrystals with the ability to select the amount of metal ion on the surface in the final product.

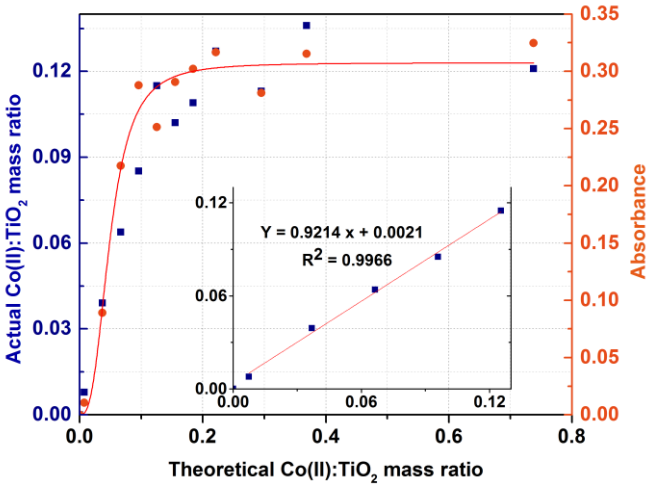

Figure 3. Actual (from elemental analyses) versus theoretical Co:TiO2 mass ratio and absorbance (λmax = 590 nm; see figure S15) versus theoretical Co:TiO2 mass ratio (inset is the linear fit of the actual Co:TiO2 mass ratio up to the surface saturation limit ~12%).

In conclusion, we have demonstrated unprecedented control of attachment of transition metal ions to the surface of well-defined inorganic nanocrystals in non-polar solvent analogous to solution atomic layer deposition. The method uses inexpensive metal chloride hydrates, and allows variable loading of the nanocrystal surface with Cr3+, Mn2+, Fe2+, Co2+, Ni2+, and Cu2+ to the point of saturation. Attachment of transition metal ions directly to the surface of the nanocrystal could allow for unparalleled new ways to self-assemble nanocrystals with coordination linkers, form well-defined single-site coordination complexes on the surface of nanocrystals, or potentially allow for unusual new monoatomic layer multi-shell nanocrystals. The location of metal ions on the nanocrystal surface may prove important in mediating electron transfer reactions that have relevance in photocatalysis or power storage. We anticipate the method could be more generally applicable to other nanocrystal compositions and morphologies, which will be the subject of future work.

Ultra-stable CdS incorporated Ti-MCM-48 mesoporous materials for efficient photocatalytic decomposition of water under visible light illumination

A state-of-the-art photocatalyst material that achieves total water splitting under visible light conditions that consists of CdS and RuO2 supported on Ti/Si MCM-48 was reported (figure 4). This approach utilizes mesoporous Ti/Si MCM-48 as a host material, and incorporate appropriate combinations of materials to achieve the functionality necessary for water splitting. Overall water-splitting efficiency was >2%; however, the quantum yield for hydrogen evolution (in the presence of methanol as electron donor) in the CdS-Ti-MCM-48 material is <16%. The data suggests that this material platform offers potential to outperform sophisticated

nanostructured catalyst materials such as Rh2-yCryO3/[(GaN)1-x(ZnO)x] discovered by Domen and co-workers as the most efficient overall water splitting catalyst. , The advantage of our system is the inherent modularity and tunability of the system.

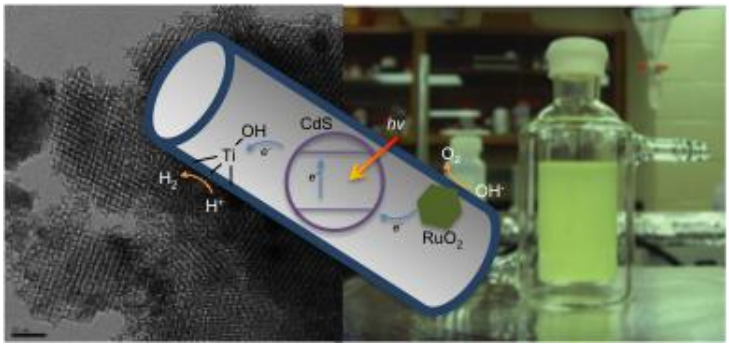

Figure 4. CdS-RuO_2-Ti-MCM48 photocatalyst material.

It was previously reported that MCM-48, with its interpenetrating 3-D pores, favours mass transfer kinetics and high dispersion of CdS. However the drawback was the lack of O2 generation and loss of CdS due to photocorrosion. In this work, CdS was incorporated into Ti-MCM-48 and loaded with the RuO2 co-catalyst12–17 and we realize generation of both H2 and O2. Most importantly, our XPS results indicate no loss of CdS after the reaction and production of H2 and O2 is sustained.

CdS incorporated into mesoporous materials have been studied before, but suffer from the following drawbacks: synthesis of mesoporous materials that are quite time-intensive (up to 7 days), and/or conducted at relatively high temperatures, use of corrosive sulfides as sacrificial agents, use of a Pt co-catalyst, very low H2 yield and absence of O2, lack of photostability studies, loss of CdS, and formation of CdO after the reaction. To the best of our knowledge, this is the first report on CdS incorporated into mesoporous silica that demonstrates visible light: (i) generation of both H2 and O2 in the absence of the Pt co-catalyst, (ii) no photocorrosion of CdS even in the absence of sulfides or sulfites, and (iii) mild conditions for preparation of CdS–Ti-MCM-48 composites. Fig. 5 presents the low angle XRD patterns of all studied samples.

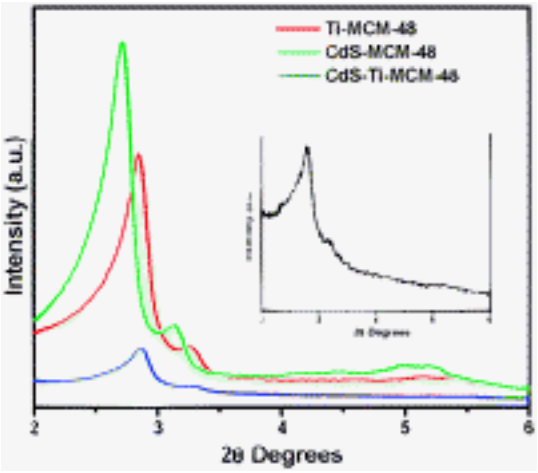

Fig. 5 Low angle XRD patterns of studied samples. The inset plot represents the RuO2–CdS–Ti-MCM-48 sample.

A characteristic Bragg reflection due to cubic Ia3d symmetry can be perceived in all samples. The strong peaks due to d211 and weak d220 reflections in the range of 2.5–3.5° demonstrate that the cubic phased mesopore structure was preserved after incorporation of TiO2, RuO2, and CdS. Moreover, the peaks, due to d321, d400, d420, and d332 in the interval of 4–6° indicate high ordered array of mesopores. Compared to the Ti-MCM-48 sample, CdS–Ti-MCM-48 and RuO2–CdS–Ti-MCM-48 exhibited less intense peaks. The decrease in peak intensity can be ascribed to the addition of CdS and/or RuO2 species that cause the lack of the scattering contrast between the pores and pore walls. The high angle XRD patterns of the samples show a broad peak at 2θ near 22.5° due to bulk silica. The absence of peaks due to TiO2, RuO2, and CdS suggests that these components are highly dispersed in MCM-48. In addition, it is possible that the extremely small size of these species precludes its detection limit of XRD. Nitrogen isotherms show a reversible isotherm of type IV indicating the mesoporous nature. The pore size distribution of all the studied samples exhibits a highly uniform material.

UV-Vis diffuse reflectance spectroscopy (DRS) is useful in evaluating the local environment of Ti4+ and determining the particle size of CdS. Fig. 6 shows the DRS spectra of all samples. In Ti-MCM-48, the strong absorption at ~210 nm is attributed to the ligand to metal charge transfer from O2− to Ti4+ in tetrahedral coordination. A broad shoulder at ~270 nm indicates the presence of a fraction of Ti4+ in octahedral geometry. The absence of a peak near 330 nm suggests that no bulk TiO2 is formed in Ti-MCM-48. Also, the absorption onsets of all Ti-MCM-48 samples are ~350 nm. This indicates that the Ti species are highly dispersed in MCM-48. Meanwhile, the position of adsorption onsets of CdS containing MCM-48 exhibits a significant blue shift (~500 nm) compared to bulk CdS (~600 nm). The blue shift in the CdS absorption onset is due to quantum confinement effects. The band gap energy of the CdS species in CdS-MCM-48 and RuO2–CdS–Ti-MCM-48 is 2.46 eV and the particle size of CdS is estimated to be ~3.4 nm from the Brus equation. Similarly,

the band gap energy of CdS in CdS–Ti-MCM-48 is 2.43 eV, and the particle size of CdS is 3.6 nm. The particle size of CdS is larger than the size of mesopores in Si- and Ti-MCM-48 materials. It is well-documented that small CdS clusters can agglomerate in porous materials including MCM-48 due to quantum tunneling effects. Nitrogen sorption (a decrease in pore volume from 0.76 to 0.66 cm3 upon loading CdS) and DRS studies indicate that most of the CdS particles are embedded in the pores of MCM-48 while a small portion of CdS deposited on the external surface of MCM-48 cannot be completely eliminated. X-ray photoelectron spectroscopy (XPS) is a sensitive tool for investigating the surface chemical composition and oxidation state. The XPS plots of CdS incorporated samples show peaks at 411.6 and 404.9 eV due to Cd 3d5/2 and 3d3/2 with a separation of 6.7 eV which is typical of CdS. The S2– 2p1/2 and 2p3/2 peaks appear at 162.4 eV and 161.2 eV and support the formation of CdS. The ratio of S2– to silica was determined to be 0.015 in the sample prior to photocatalytic reaction.

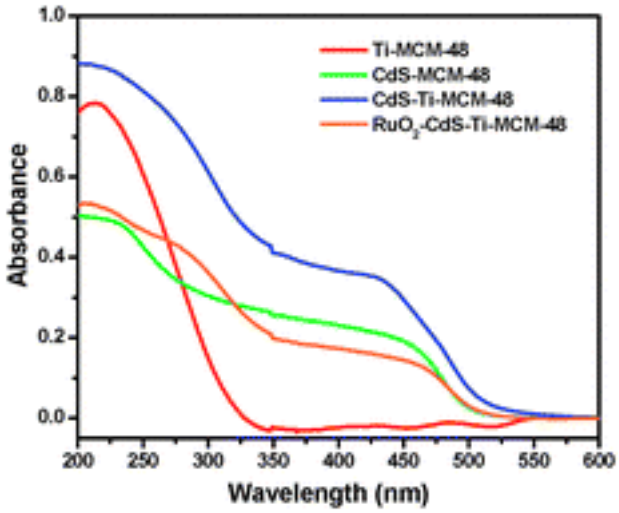

Fig. 6 Diffuse reflectance spectra of MCM-48 samples.

The photocatalytic H2 and/or O2 evolution rate and the apparent quantum yield (AQY) are listed in Table 1. Ti-MCM-48 does not generate H2 and O2 under visible light. In contrast, all the CdS containing MCM-48 photocatalysts exhibit a significant amount of H2. Compared to the H2 production generated by the CdS-MCM-48 sample (0.22 mmol h−1 gcatalyst−1), CdS–Ti-MCM-48 gives a higher H2 evolution rate (2.73 mmol h−1 gcatalyst−1). This remarkable increase in the photocatalytic activity is mainly due to the presence of well dispersed TiO2 clusters that facilitate transfer of electrons from the c.b. of CdS to TiO2 in CdS–Ti-MCM-48, thus minimizing electron–hole recombination. Also, the valence band (v.b.) edge of TiO2 clusters is more positive than the v.b. of CdS and hence, holes in the v.b. of CdS cannot diffuse to the TiO2 v.b. TEM images of CdS–Ti-MCM-48 and RuO2–CdS–Ti-MCM-48 show the cubic phase is seen along with some dark contrasts. At high magnifications one can see lattice fringes. Careful examination of the fringes indicates the presence of RuO2 with a d200 spacing of 2.43 Å. In addition, lattice

fringes due to CdS and TiO2 are also seen with a d101 spacing of 3.13 Å and a d101 spacing of 3.54 Å, respectively. As stated previously, the particle size of CdS estimated from DRS studies is ~3.4 nm and the particle size of RuO2 estimated from TEM studies is ~7.5 nm. Energy Dispersive X-ray Spectroscopic (EDS) studies show the distribution of the various elements. In addition, EDS mapping results indicate the close contact of RuO2 particles with CdS and TiO2. The fairly high dispersion of titania in the silica support is also observed.

Table 1 Photocatalytic activities of MCM-48 materials

Sample	H2 rate (mmol h−1 gcatalyst−1)	O2 rate (mmol h−1 gcatalyst−1)	AQY
Ti-MCM-48	0	0	0%
CdS-MCM-48	0.22	0	2.9%
CdS–Ti-MCM-48	2.73	0	36.3%
RuO2–CdS–Ti-MCM-48	0.26	0.13	3.5%

Interestingly, in RuO2–CdS–Ti-MCM-48, the stoichiometric ratio of H2 (1.56 mmol) and O2 (0.75 mmol) was achieved by utilizing visible light in the presence of ethanol after 6 h of irradiation. Alcohols such as ethanol have been employed as sacrificial electron donors and higher H2 yields have been observed since they can be easily photooxidized. We have detected acetaldehyde in our experiments (but have not quantified them) since it is not the focus of our work. Surprisingly, in the presence of a hole transfer agent, i.e. in RuO2–CdS–Ti-MCM-48, we also observe O2. RuO2 is a very active catalyst for O2 evolution because of its low overpotential. In ethanolic solutions, the holes produced in the v.b. of CdS can migrate to the surface of the photocatalyst and oxidize ethanol and may also be trapped at the surface by RuO2 to produce O2 and it seems that the trapping of the holes by RuO2 is fairly efficient in our system since stoichiometric amounts of O2 were formed. Thus, the presence of ethanol (sacrificial electron donor) and RuO2 (low overpotential for O2 generation) help in the formation of both hydrogen and oxygen. In the presence of pure water under identical conditions, RuO2–CdS–Ti-MCM-48 forms stoichiometric amounts of H2 (0.72 mmol gcatalyst−1) and O2 (0.35 mmol gcatalyst−1) after 6 h of irradiation indicating the role of RuO2 in generating O2 but with lower yields as expected.

To investigate the stability of RuO2–CdS–Ti-MCM-48, recycling studies were carried out. Fig. 7 shows the photocatalytic H2 and O2 rate of RuO2–CdS–Ti-MCM-48 in ethanol. The results indicate that RuO2–CdS–Ti-MCM-48 is extremely robust and its photocatalytic activity is sustainable. However, RuO2–CdS–Ti-MCM-48 shows a significant decrease in the H2 evolution rate (0.26 mmol h−1 gcatalyst−1) compared to CdS–Ti-MCM-48. The decrease in H2 yield is probably due to RuO2 species that also act as recombination centres of the photogenerated electron–hole pairs. Also, the loading sequence of RuO2 is prior to CdS into Ti-MCM-48, and thus, the RuO2 clusters may preclude intimate contact between CdS and TiO2. In addition, the higher absorbance of CdS–Ti-MCM-48 in comparison to RuO2–CdS–Ti-MCM-48 may also be a factor responsible for enhanced hydrogen production in CdS–Ti-MCM-48. In order to elucidate the photoinduced charge carrier transfer pathways in CdS–Ti-MCM-48 samples, the electron paramagnetic resonance (EPR) study was carried

out. Irradiation of CdS by visible light leads to the production of electron–hole pairs. As suggested previously, electrons promoted to the c.b. in CdS can be injected into TiO2. EPR signals were monitored by irradiating the sample with visible light (cut off filter 400 nm) in the presence of glycerol. The EPR spectrum of CdS–Ti-MCM-48 indicates the formation of Ti3+ ($g_\perp$ = 1.958 and $g_\parallel$ = 1.920), which is evidence for electron transfer from CdS to TiO2. A strong signal near g = 2.004 is due to organic radicals formed by the reaction of photogenerated holes with glycerol.23 A stronger Ti3+ peak is found for CdS–Ti-MCM-48 compared to that for the RuO2 containing sample as seen in the EPR plot. Hence, efficient transfer of electrons from CdS to TiO2 is prevented and H2 production diminished. Most importantly, XPS studies of CdS–Ti-MCM-48 samples do not show any loss of CdS after the photocatalytic reaction (the ratio of S2− to silica in the spent catalyst remains to be 0.015) even though the reaction was carried out in the absence of sulfides and sulfites as sacrificial agents. Also, in the XPS plots of the spent catalysts, CdS shows peaks at 411.6 and 404.9 eV due to Cd 3d5/2 and 3d3/2 and S2− 2p1/2 and 2p3/2 peaks at 162.4 eV and 161.2 eV that indicate the retention of CdS. The intensities of Cd and S in the fresh and spent samples remain virtually unchanged indicating the high stability of CdS after encapsulation in the MCM-48 matrix. Our AAS results also confirm the retention of CdS in RuO2–CdS–Ti-MCM-48 after long-term photocatalytic reaction and indicate no loss of CdS. The generation of O2 also indicates that the holes produced in the v.b. of CdS do not cause photocorrosion and that oxidation of water occurs as suggested previously.

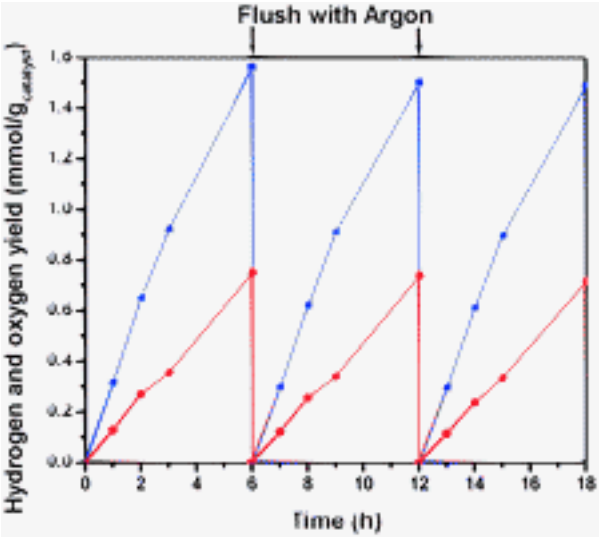

Fig. 7 Photocatalytic water splitting over RuO2–CdS–Ti-MCM-48. Blue squares and red circles denote H2 and O2.

b. immobilization of hybrid nanocrystals in membranes

The vision in this component was to immobilize heteronanocrystals into self-assembled membranes; however, the preparation of inorganic nanocrystals became the major focus of the work. A composite material with organic membrane and

inorganic nanostructures was never produced. However, this remains an important goal in future work. Instead, membranes composed of TiO2 nanotube arrays were prepared.

Synthesis of ordered mesoporous TiO2 thin-film was performed using Evaporation Induced Self Assembly (EISA) and supercritical CO2 assisted infusion methods. In EISA, a dilute solution containing Ti-butoxide, Pluronic123, HCl (38% in water), and butanol was spin coated on a glass substrate. The coated substrates were aged for 24 hr in a controlled humidity environment at 25C. Films after aging were calcined at 350C for 2 hr to remove the surfactant. In supercritical CO2 infusion method, a glass substrate pre-coated with the Pluronic F108 surfactant film was loaded inside a PARR reactor, and it was heated to 60C and pressurized to 3000 psi with CO2. At these processing conditions, a known amount of Ti-butoxide followed by water was injected into the reactor. As a result, solubilized portion of Ti-precursor in supercritical CO2 was infused and hydrolyzed inside the solid surfactant film coated on a substrate. After 1 hr, the reactor was depressurized and cooled down to room temperature and the substrates were removed and calcined at 350C. The films synthesized by both methods were characterized by SEM, AFM, XRD, BET surface area, and ellipsometry. SEM images of TiO2 film prepared by EISA as shown in Figure 8a&b reveal ordered mesoporous structure with 3D cubic and 2D hexagonal pore ordering with the d-spacing of 18.50 nm and 18 nm, respectively as determined by FFT analysis. AFM images as shown in Figure 8c &d represent the scan area of 1000 nm^2, which indicate highly ordered structure of the mesopores. Figure 9a&b indicates partial pore ordering in the TiO2 thin-films synthesized using supercritical CO2 assisted infusion. The smaller size pores as evident in SEM and AFM images may provide mass transfer limitation for charge transport. Consequently, experiments were performed to increase pore size using pore swelling agent; for instance, 1,3,5 trimethyl benzene (TMB). From Figure 9c&d, we can easily observe increase in pore volume and surface area for the TiO2 prepared using TMB at different concentration levels. Crack free ordered mesoporous TiO2 thin films with different thickness were prepared using EISA method. Table 1 shows the thickness and refractive index (RI) of films with multiple spin coats between with 5 to 35. Thickness and RI was determined by fitting optical constants from experimental data obtained from a discrete wavelength ellipsometry with Cauchy model. The film thickness ranges from 400 nm to 3100 nm depending on number of layers coated and the average refractive index for these films was 1.5 as determined by ellipsometry.

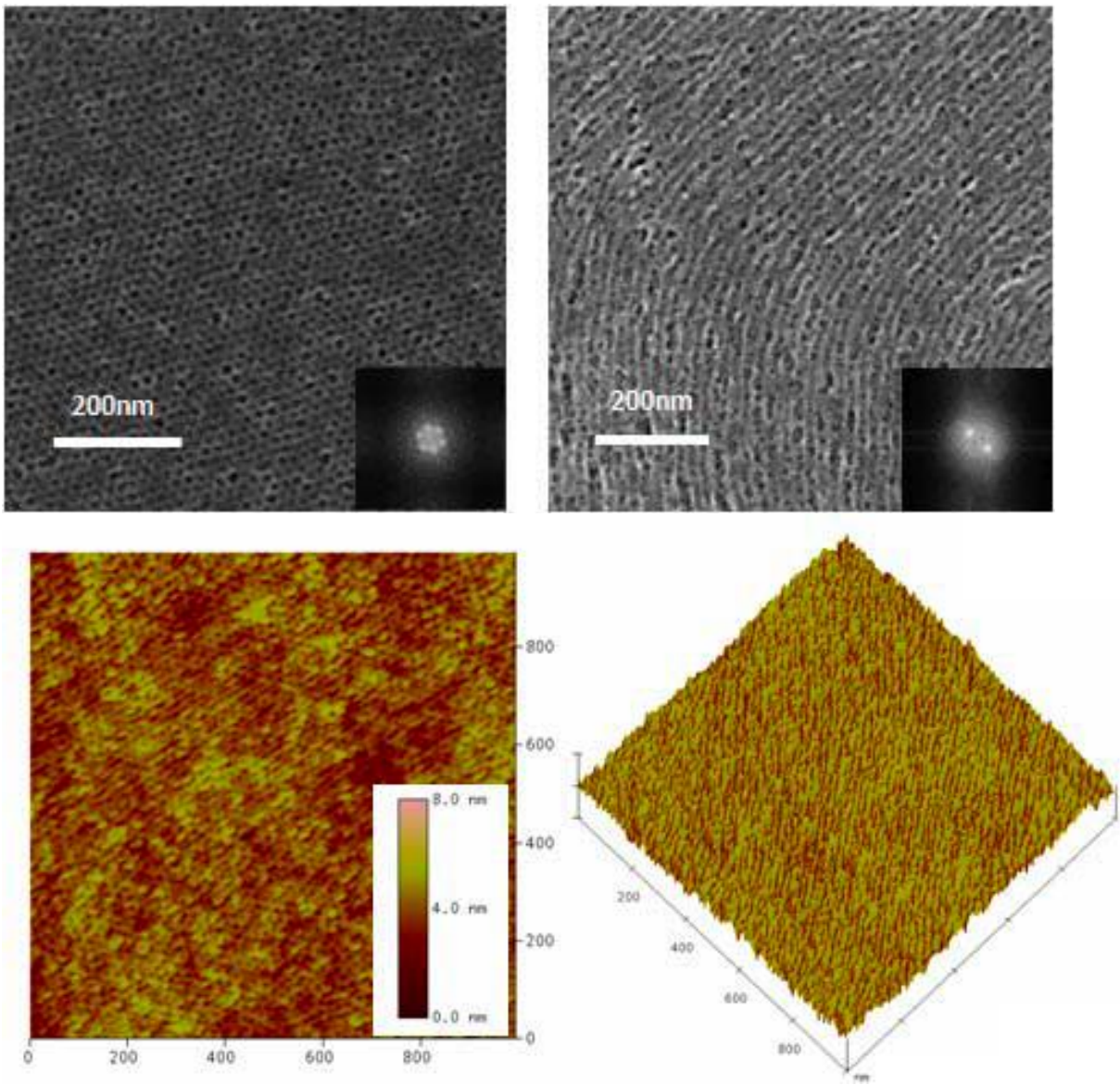

Figure 8: SEM and AFM images of ordered TiO2 film prepared by EISA (a: 3D cubic pores, b: 2D hexagonal pores, c: 1mm2 scan of highly ordered TiO2 film on glass substrate, and d: film topography in 3D).

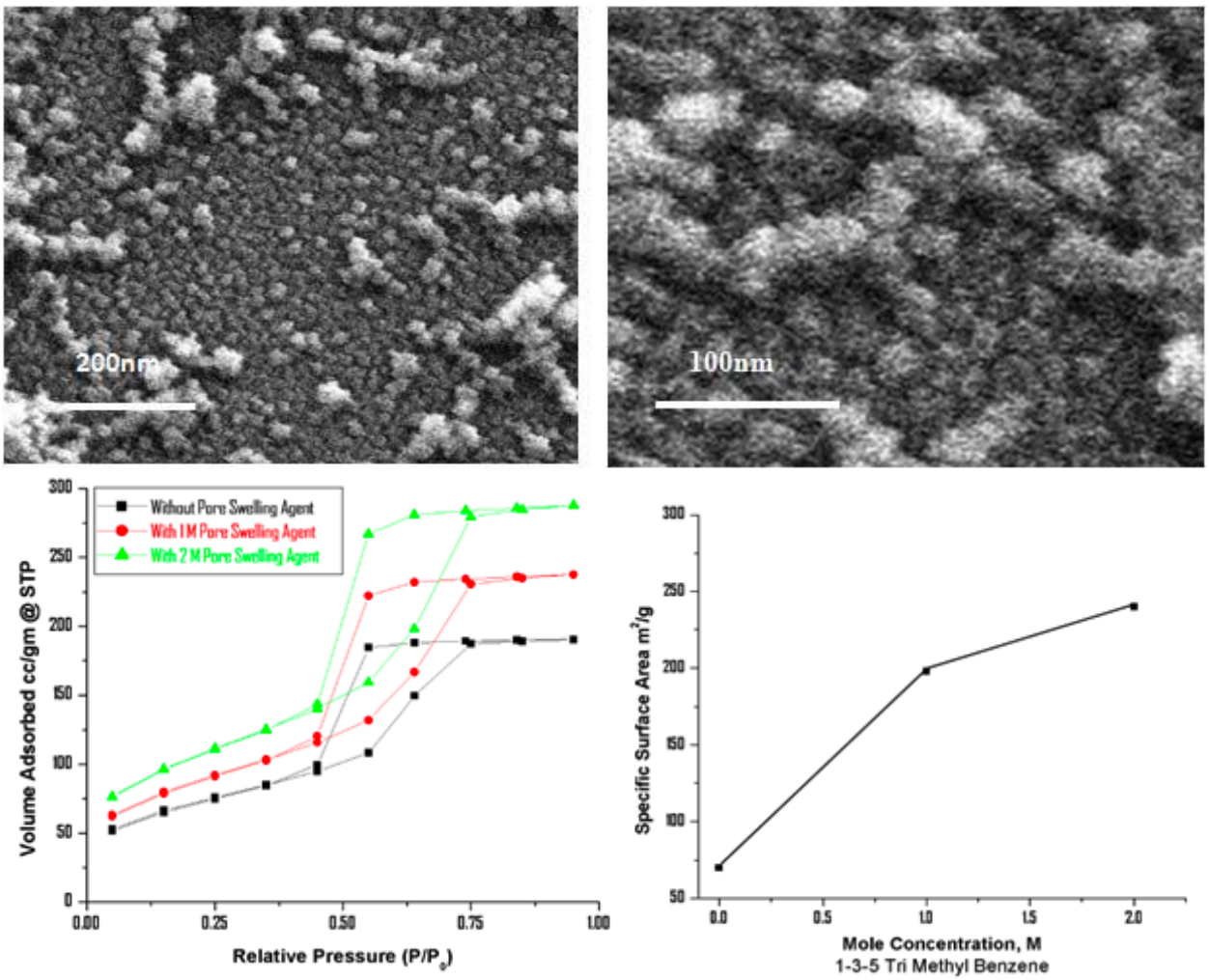

Figure 9. SEM images of ordered TiO2 film prepared by supercritical CO2 infusion method (a: surface topology, b: average pore size of 4 nm), c) N2 adsorption and desorption isotherms of TiO2 prepared by EISA in presence of TMB and d) BET specific surface area.

Efforts were made on the fabrication of double sided TiO_2 nanotube membrane using electrochemical anodization method. Double sided TiO_2 nanotubes were grown using Ti foil (25μm thick, 99.7%purity) purchased from Alfa Aesar. Ti sheet was degreased by sonicating sequentially in acetone, ethanol, and de-ionized water, followed by drying in a nitrogen stream. Electrochemical anodization of titanium was carried out at ambient conditions using a two-electrode system and a DC power supply (Agilent Technologies, 0-60V). Degree of anodization of Ti metal was controlled by limiting anodization voltage and H_2O content in the electrolyte. For anodization an organic electrolyte containing 0.3wt% NH_4F and 2vol% water in ethylene glycol was used. A platinum gauge electrode was used as a cathode in all the experiments. After anodization, the sample was washed in water to remove the impurities. The double sided TiO_2 nanotubes membrane was sensitized with 0.1 M dilute aqueous salt solution of hexachloroplatanic acid and sonicated for 5 minutes

and finally annealed in argon environment containing 10 vol% H_2 at 400°C for 1 hr. The SEM image of annealed Pt/TiO_2 nanotubes is shown in Figure 10A whereas SEM image for the cross section of double sided TiO_2 nanotube membrane is depicted in Figure 10B. These images revealed tube length of about 17μm on both side of etched Ti metal foil.

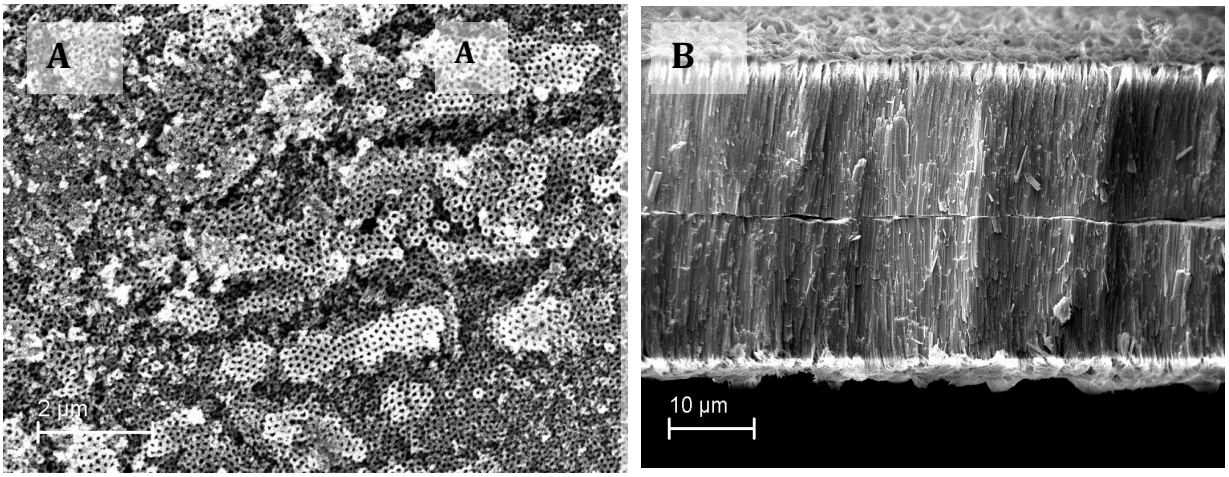

Figure 10: SEM images of **A)** TiO_2 nanotubes sensitized with Pt and **B)** cross section of double sided TiO_2 nanotubes membrane.

1c. characterization of nanocomposite material with sum-frequency generation spectroscopy

A nanocomposite material composed of organic membrane with oriented inorganic nanocrystals was envisioned. Ultimately, such a material was not produced over the course of the project, and therefore no SFG characterization was made.

1d. utilize ceramic capillaries as support of nanocomposite membranes

A nanocomposite material composed of organic membrane with oriented inorganic nanocrystals was envisioned. Ultimately, such a material was not produced over the course of the project, and therefore was not deposited on ceramic capillaries as outlined in the project proposal. A competing strategy; however, was to prepare double-membrane TiO2 nanotube arrays (see objective 1b above).

2. Electrospun carbon nanofelts as supports for improving performance of fuel cells

2a. Preparation and Characterization of the Electrospun Carbon Nanofelt Made from PAN and/or PVA Nanofiber Nanofelt Precursors

2b. Fabrication and Evaluation of the Prototype Fuel Cells Made of the Electrospun Carbon Nanofelt, Investigation on Durability (in-situ Oxidation/Degradation) of the Prototype Fuel Cells

In this proposed research, nonwoven fabrics made of electrospun polyacrylonitrile (PAN) polyvinyl alcohol (PVA), and titanium carbide (TiC) based carbon nanofibers, dubbed as Electrospun Carbon Nanofelt, with extremely high specific surface areas (up to 2,200m^2/g) and other desired morphological and structural properties (e.g. high graphitic crystallinity) were investigated.

Preparation and Characterization of the Electrospun Carbon Nanofelt made from PAN and/or PVA Precursors.

We investigated electrospinning in the controllable environment that involved understanding the effects of environmental conditions (e.g. solvent vapor pressure, temperature, humidity), as well as solution characteristics (e.g. viscosity, conductivity, and surface tension coefficient) and process variables (e.g. electrostatic field, flow rate, power and polarity of high voltage supply) on the electrospinning process, and on the morphologies, structures and properties of PAN, PVA and TiC nanofibers.

We studied the thermal processes (i.e., stabilization, carbonization, graphitization and activation) on the properties of electrospun PAN and/or PVA based carbon nanofibers, and identified the optimal conditions/procedures of the thermal processes to prepare the electrospun carbon nanofelt with extremely high specific surface areas and other desired morphological and structural properties (e.g. high graphitic crystallinity).

We studied the treatment process to convert TiC nanofibers into extremely porous carbon nanofibers. identify the optimal processing conditions to prepare the electrospun carbon nanofelt with extremely high specific surface areas and other desired morphological and structural properties (e.g. high graphitic crystallinity).

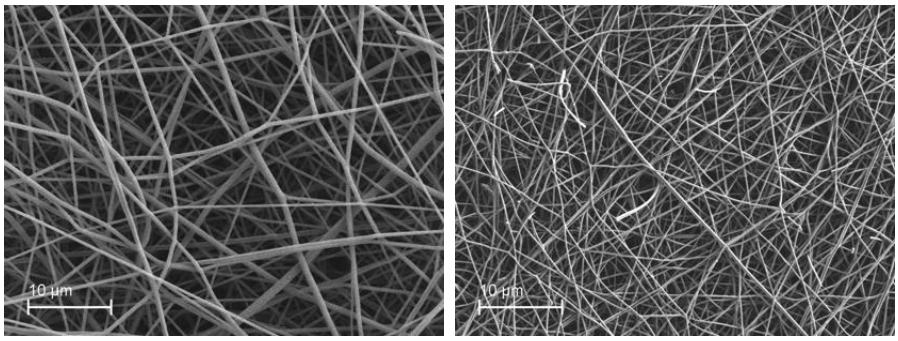

Figure 11. PAN based electrospun nanofibers (left) and PAN-based carbon nanofibers (right).

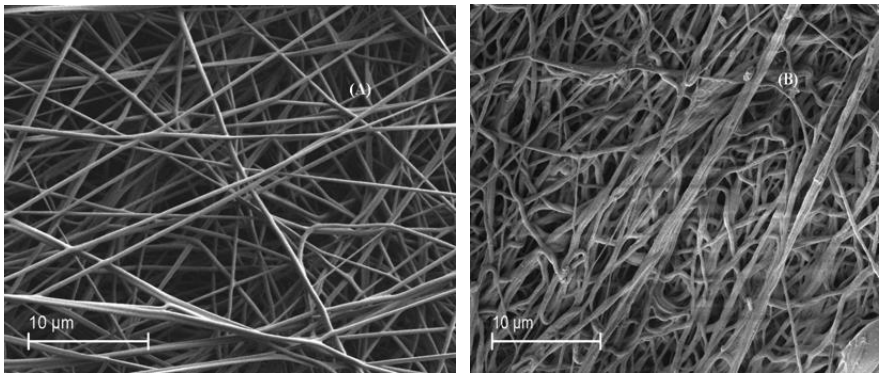

Figure 12. PVA based electrospun nanofibers (left) and PVA-based carbon nanofibers (right).

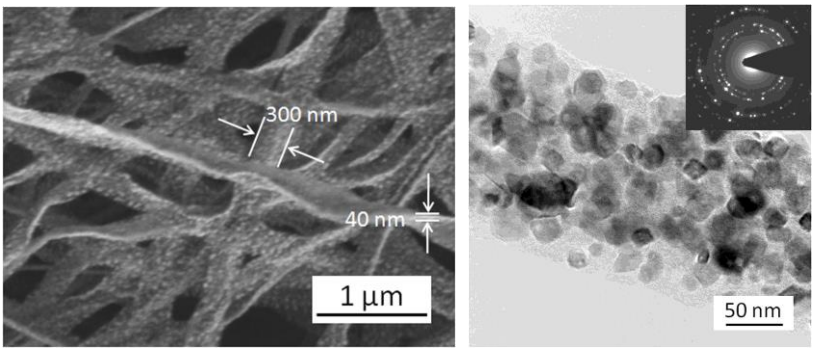

Figure 13. Continuous titanium carbide (TiC) nanofibers that possessed the intriguing nanoribbon morphology with width and thickness being ~300 nm and ~40 nm, respectively, and contained TiC crystallites with sizes ranging from 5 nm to 30 nm were synthesized through electrospinning followed by carbothermal reduction.

Electrospun TiC nanofibers were synthesized and woven into mats. The electrospun TiC nanofibers in the form of overlaid fiber-mat could be an innovative precursor for the development of carbide derived carbon (CDC) with exceptionally large pore volume and specific surface area, which would be particularly useful for the applications such as catalyst support, gas storage, super-capacitor, and phase change material support in thermal management systems (figures 14-23).

Development of the carbide derived carbon with high specific surface area based upon the electrospun TiC nanofibers and/or nanoribbons

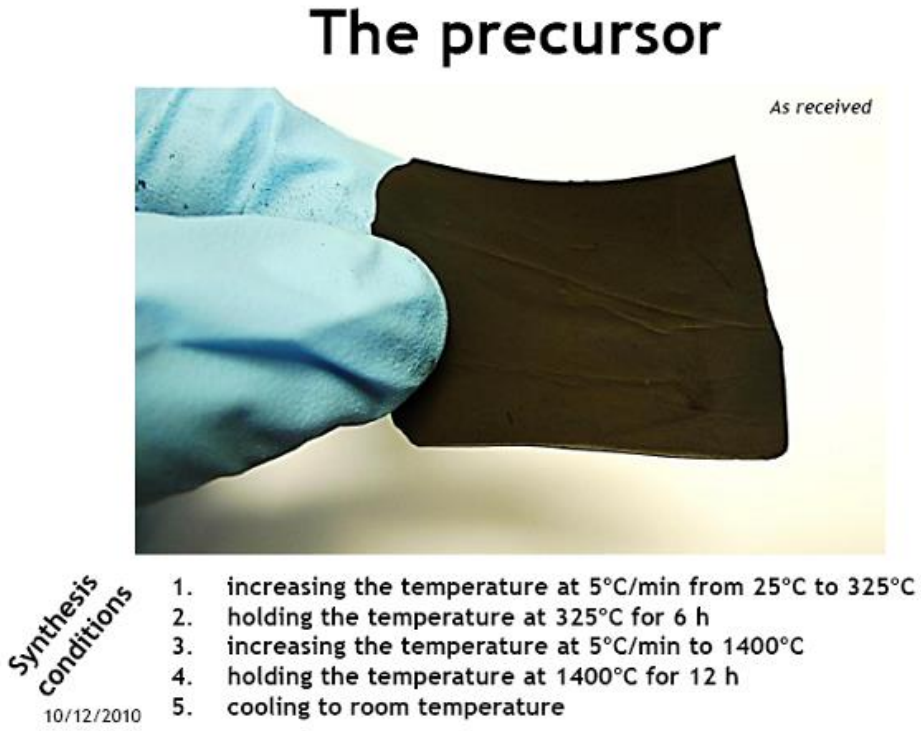

Figure 14. TiC nanofelt.

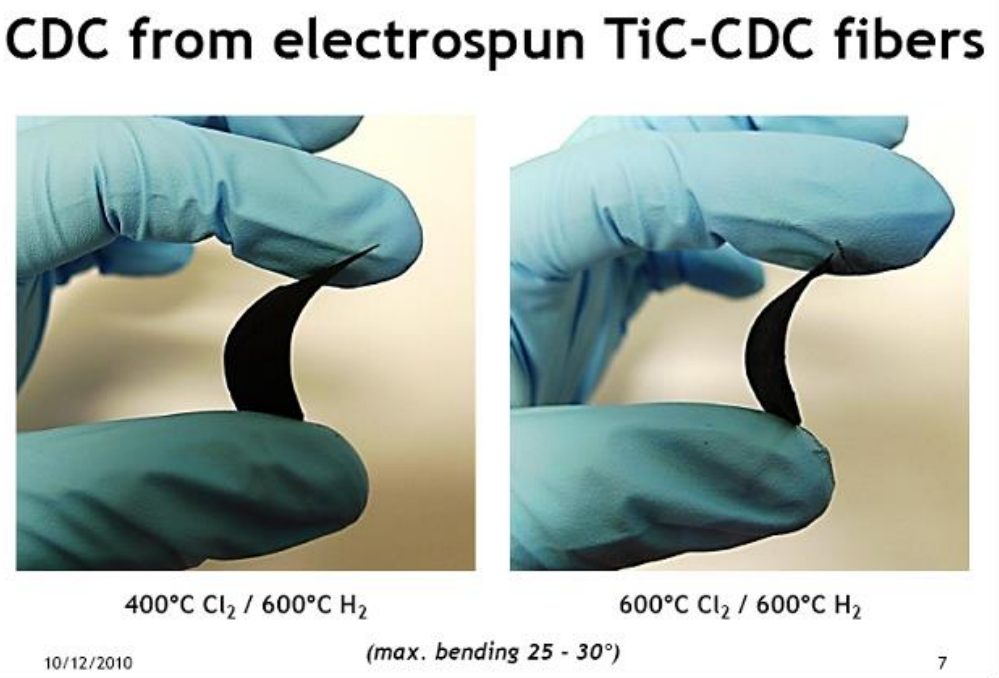

Figure 15. Carbide-derived carbon (CDC) nanofelt.

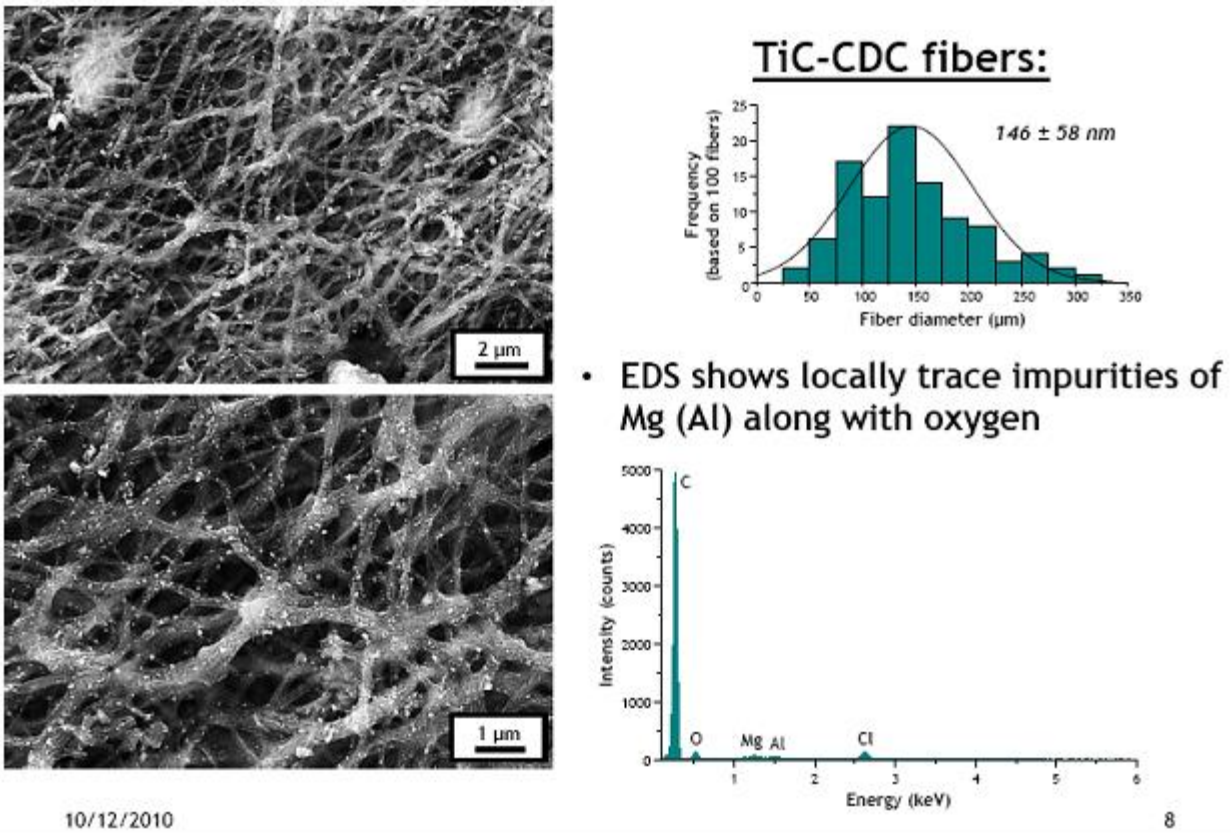

Figure 16. SEM images of TiC-CDC (400°C)

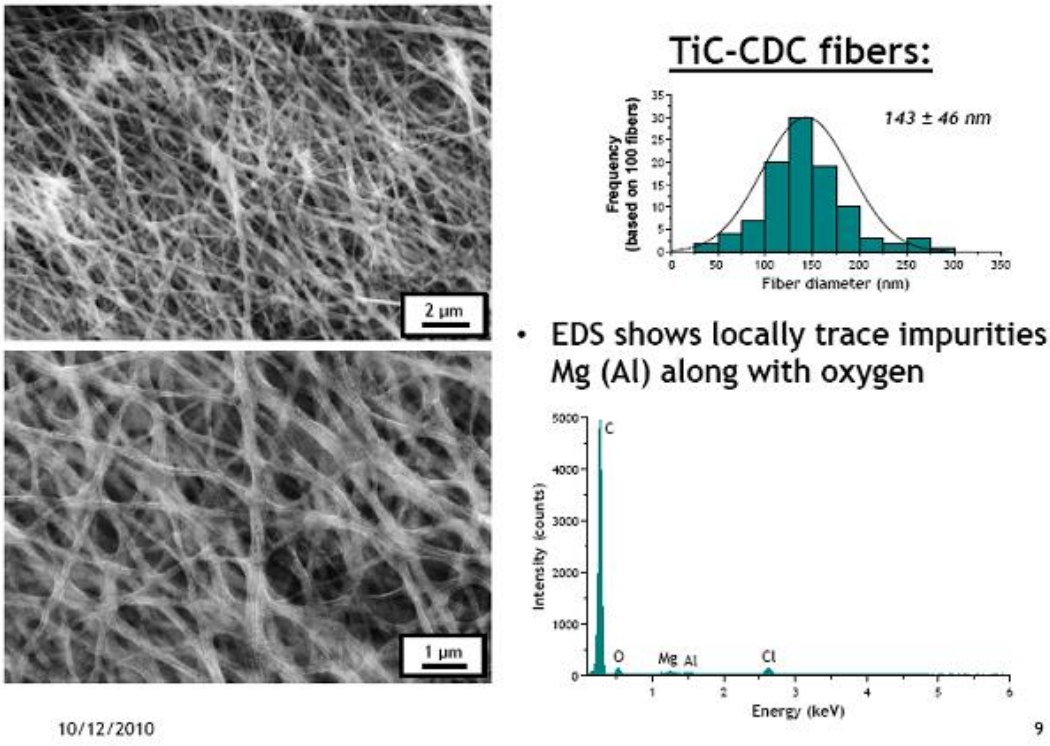

Figure 17. SEM images of TiC-CDC (600°C)

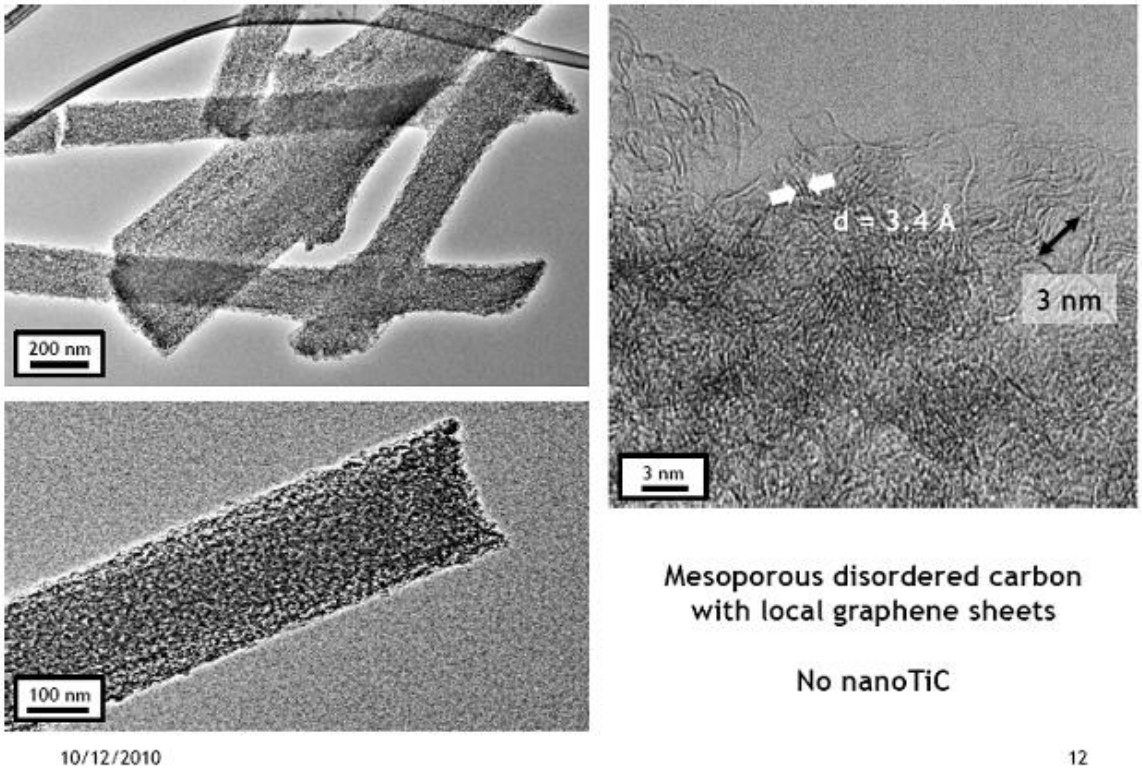

Figure 18. TEM images of TiC-CDC (400°C)

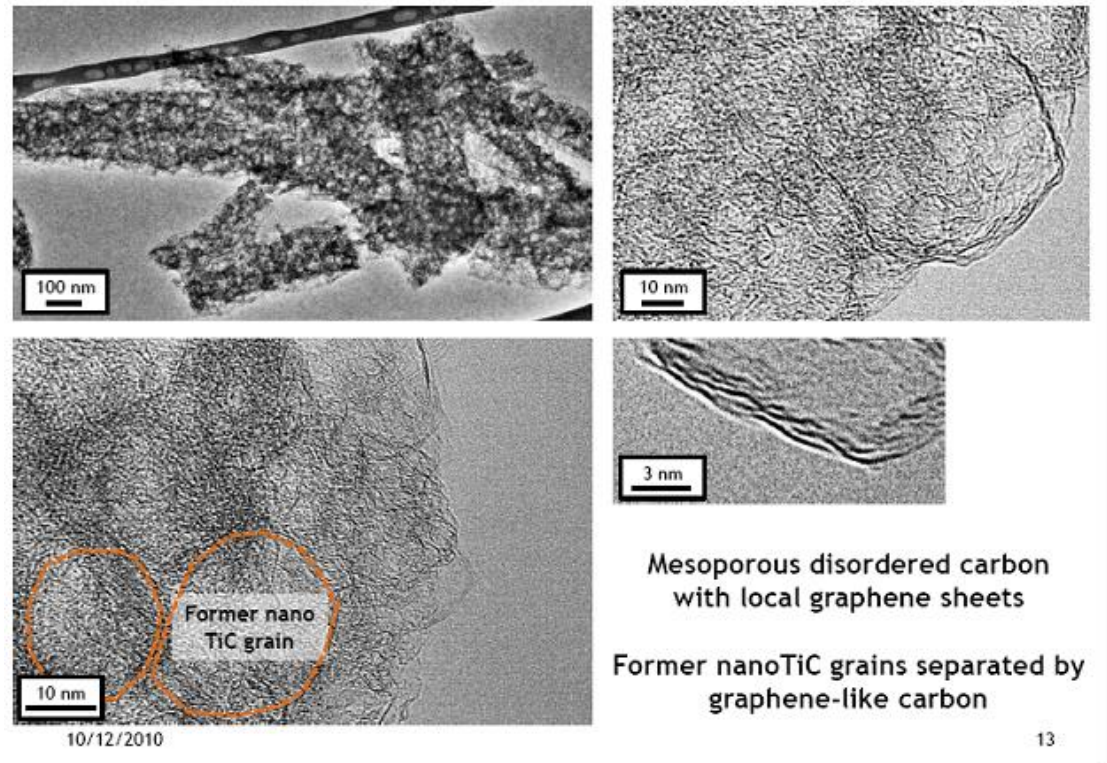

Figure 19. TEM images of TiC-CDC (600°C)

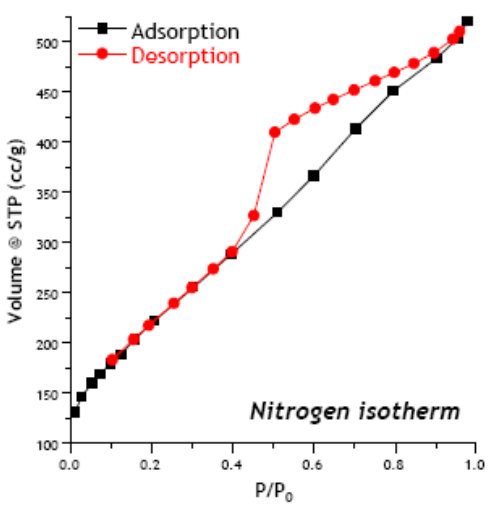

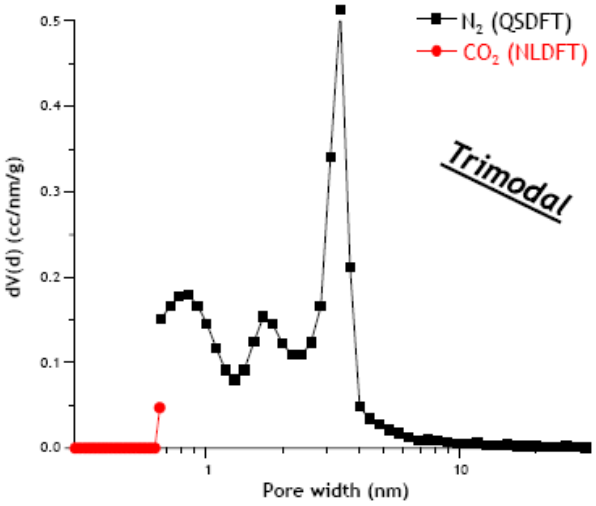

	SSA (m^2/g)				Pore volume (cc/g)			Mean
	BET (N_2)	PSD (N_2: > 0.6 nm)	PSD (CO_2: < 0.6 nm)	PSD total	Pore volume (N_2: > 0.6 nm)	Pore volume (CO_2: < 0.6 nm)	Total pore volume	width (nm)
Precursor	*738*	*682*	*4*	*686*	*0.75*	*0.01*	*0.76*	*1.6*

Figure 20. Gas sorption: TiC-CDC (400°C)

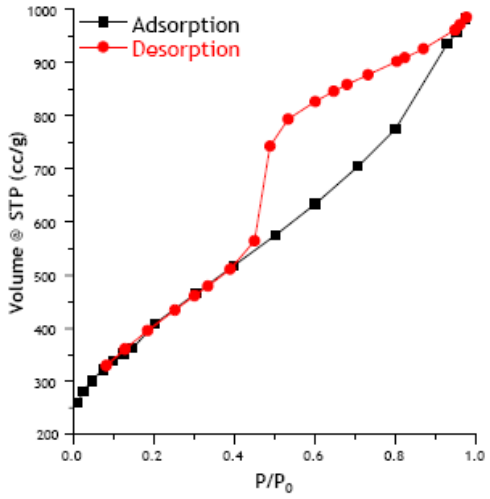

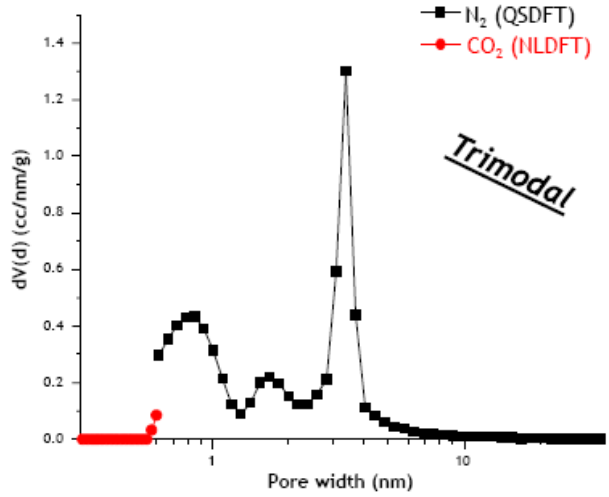

	SSA (m^2/g)				Pore volume (cc/g)			Mean
	BET (N_2)	PSD (N_2: > 0.6 nm)	PSD (CO_2: < 0.6 nm)	PSD total	Pore volume (N_2: > 0.6 nm)	Pore volume (CO_2: < 0.6 nm)	Total pore volume	width (nm)
Precursor	*1390*	*1309*	*10*	*1319*	*1.43*	*0.08*	*1.51*	*1.6*

Figure 21. Gas sorption: TiC-CDC (600°C)

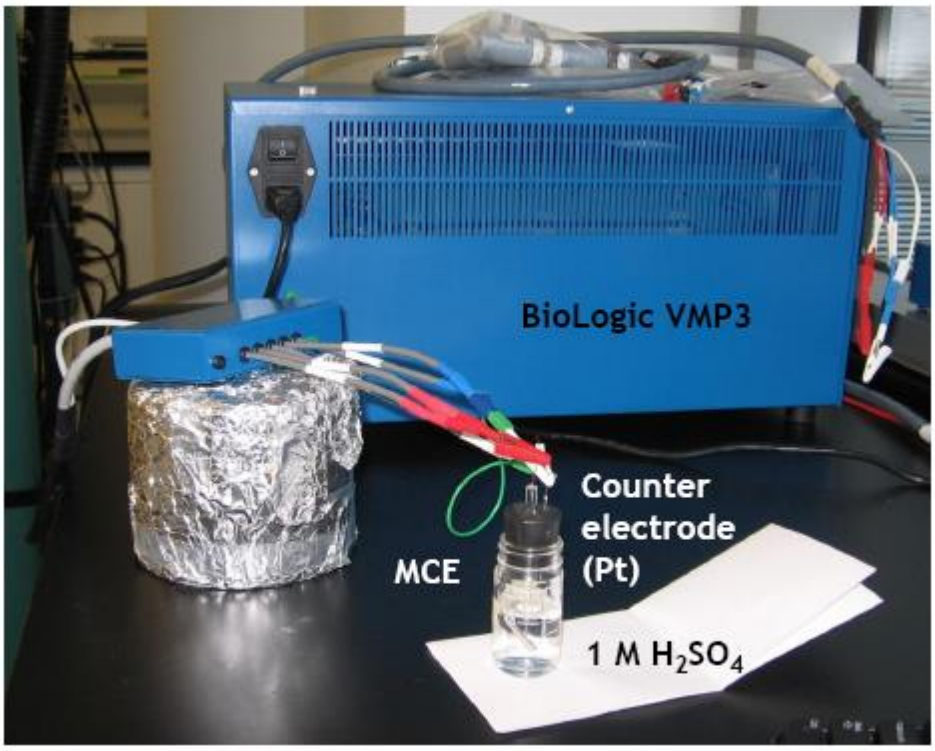

MCE... Micro-Cavity-Electrode

Figure 22. Electrochemical testing of TiC-CDC fibers.

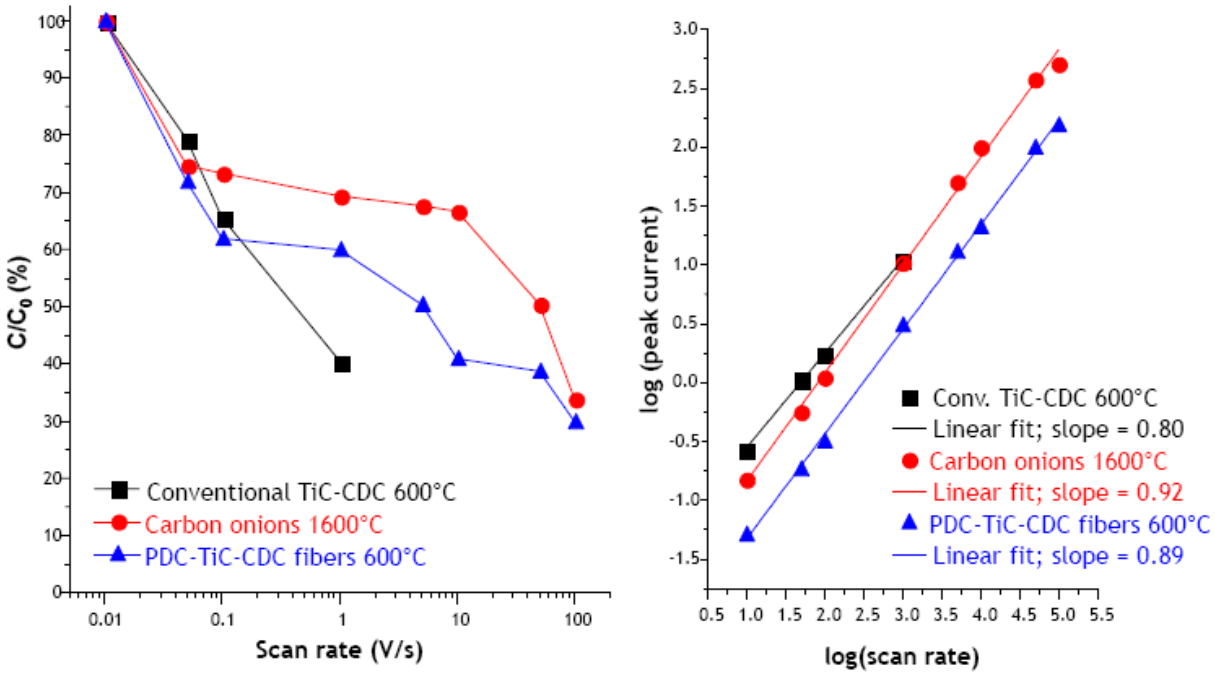

Figure 23. MCE testing in 1 M H_2SO_4

2. Synthesize Nanocrystal Catalyst

Most of the fuel cell work centered on the synthesis of graphitic supports based on electrospun carbon fibers and testing the properties of these materials. The group has recently been expanded to add to the team capabilities. One strategy will be to use super-critical CO_2 reaction systems to synthesize metal nanoparticle catalysts that can be formulated into an ink that can be applied to the fuel cell support material.

3. Develop and test prototype fuel cell

Preparation of Electrospun TiC nano-fibrous felts

The TiC nano-fibrous felts were prepared by electrospinning of a spin dope containing n-butoxide (TiBO) and furfuryl alcohol (FA) followed by carbothermal reduction in argon (first at 325 °C and then at 1400 °C). The detailed preparation procedures and conditions were described in a previous publication.

Preparation of TiC-CDC nano-felts

TiC-CDC nano-felts were prepared by chlorination of the electrospun TiC nano-fibrous felts to remove Ti at elevated temperatures, and the detailed procedure was described in a previous publication. For chlorination, the precursor was placed into a horizontal fused-quartz tube furnace, purged with argon, heated to 400 or 600 °C with a constant rate of 2 °C/min, and then exposed to dry chlorine gas (10-15 cm^3/min) for 6 hrs. After chlorination, the samples were kept at 600 °C for 2 hrs under flowing hydrogen gas to remove residual chlorine and chlorides trapped in the pores.

Structural Characterization

A Zeiss Supra 50VP field-emission scanning electron microscope (SEM) and a JEOL 2010 transmission electron microscope (TEM), both equipped with energy dispersive X-ray spectrometer (EDS), were employed to examine morphological and structural properties of the developed TiC-CDC nano-felts and their precursor of electrospun TiC nano-fibrous felts. The SEM and TEM were operated at 10 kV and 200 kV, respectively. The SEM specimens were analyzed without sputter coating of metals or carbon, since the samples were electrically conductive and would not result in charge accumulation. The TEM specimens were prepared by dispersing samples in ethanol followed by placing the suspensions over copper grids with lacey carbon film.

Raman spectra were recorded with a Renishaw micro-spectrometer using an argon-ion laser (488 nm, ~1 μm lateral spot size). The analyses of two main Raman active modes of disordered carbon (D-band at ~1340 cm^{-1} and G-band at ~1600 cm^{-1}) were carried out by deconvolution. The X-ray diffraction (XRD) analyses were carried out using a Rigaku diffractometer with Cu-Kα radiation (λ = 1.5406 Å) operated at 30 mA and 40 kV. The XRD patterns were collected using step scans with the step of 2θ being 0.01° and the count time of 2 s per step between the 2θ of 10° and 80°. The calculation of the mean coherence length (corresponding to the

mean domain size) was performed using the TOPAS4 (Bruker AXS) based on whole-pattern Rietveld refinement. The contribution from the instrument function was corrected following the fundamental parameter approach (FPA) by measuring the reference sample of corundum.

Prior to gas sorption analysis, all samples were degassed at 200 °C in low vacuum (0.2 torr) for 24 hrs to remove the adsorbed species. Gas adsorption analyses using N_2 (at -196 °C) and CO_2 (at 0 °C) as adsorbates were conducted with the Quadrasorb surface area and pore size analyzer (Quantachrome Instruments). With the combined information from N_2 sorption (covering the range of 1-50 nm) and CO_2 sorption (0.35-1.5 nm), the PSD and SSA of micro- and meso-porosities were calculated. Assuming slit-shaped pores, the non-local density functional theory (NLDFT) and the quenched solid density functional theory (QSDFT) were used for CO_2 sorption and N_2 sorption, respectively. With a type H2 hysteresis, only the adsorption branch was used for calculation of the PSD from N_2 sorption.

Electrochemical Characterization

Using a micro-cavity electrode (MCE), the characterization of electrochemical properties was conducted in 1 M H_2SO_4. The fabrication of this MCE followed a reported procedure. The MCE had a cavity with the diameter of 125 μm and the depth of 35 μm, and a platinum wire was used as the counter electrode. Thorough and reiterative filling of the cavity prior to electrochemical testing ensured complete filling of the cavity with sample material. The volumetric capacitance was calculated from cyclic voltammograms (CVs) with normalizing by the cavity volume. Cyclic voltammetry was performed by varying the scanning rates between 10 mV/s and 100 V/s with a voltage window of 0.1 to 0.5 V and with the number of cycles performed varying between 20 and 100.

In addition to MCE testing, symmetrical two electrode cells were assembled with stainless-steel current collectors and a Gore™ PTFE separator. The experiments were carried out in 1 M H_2SO_4 aqueous solution (5x5 mm^2 cell) and 1.5 M TEA-BF_4 solution (15x20 mm^2 cell) using acetonitrile as the solvent. The nano-felt was used as is without the addition of any polymeric binder and directly placed on the stainless-steel current collectors. Time constants and frequency dispersion was analyzed via impedance spectroscopy.

Results and Discussion

Structure

The chlorination treatment selectively extracted Ti from the electrospun TiC nanofibers, resulting in the formation of micro-porous carbon nanofibers. The chlorination of TiC is governed by the following equation:

$$TiC + 2Cl_2 \rightarrow TiCl_4 + C \qquad (1)$$

Unlike titanium, carbon does not react with chlorine to significant extent at 400 and 600 °C. Since electrospun TiC nanofibers contained carbon in the matrix, which could not be removed during chlorination, the precursor of electrospun TiC nano-felts were converted conformally into the TiC-CDC nano-felts.

Electrospun TiC nanofibers had the average diameter of 131 ± 52 nm, as shown in Fig. 24a, and the nano-felts were made of randomly overlaid TiC nanofibers. The latter consisted of TiC nanocrystallites embedded in a continuous matrix of disordered carbon and amorphous TiC, as evidenced by electron diffraction and high-resolution TEM (Fig. 24b-c). High-resolution TEM also revealed that the TiC nanocrystallites were surrounded by a few layers (shells) of graphitic carbon. Based on thermogravimetry and image analyses, the amount of disordered carbon in the TiC nanofibers was 25-30 wt.%. XRD data (Fig. 24d) shows broadened Bragg reflections that are in agreement with randomly distributed TiC nanocrystallites. Based on whole-pattern fitting, the average coherence length (corresponding to the mean domain size) of 21 nm was calculated; and the Rietveld analysis showed no residual strain in the crystallites. This value is consistent with the average size of TiC nanocrystallites observed from TEM images (23 ± 9 nm).

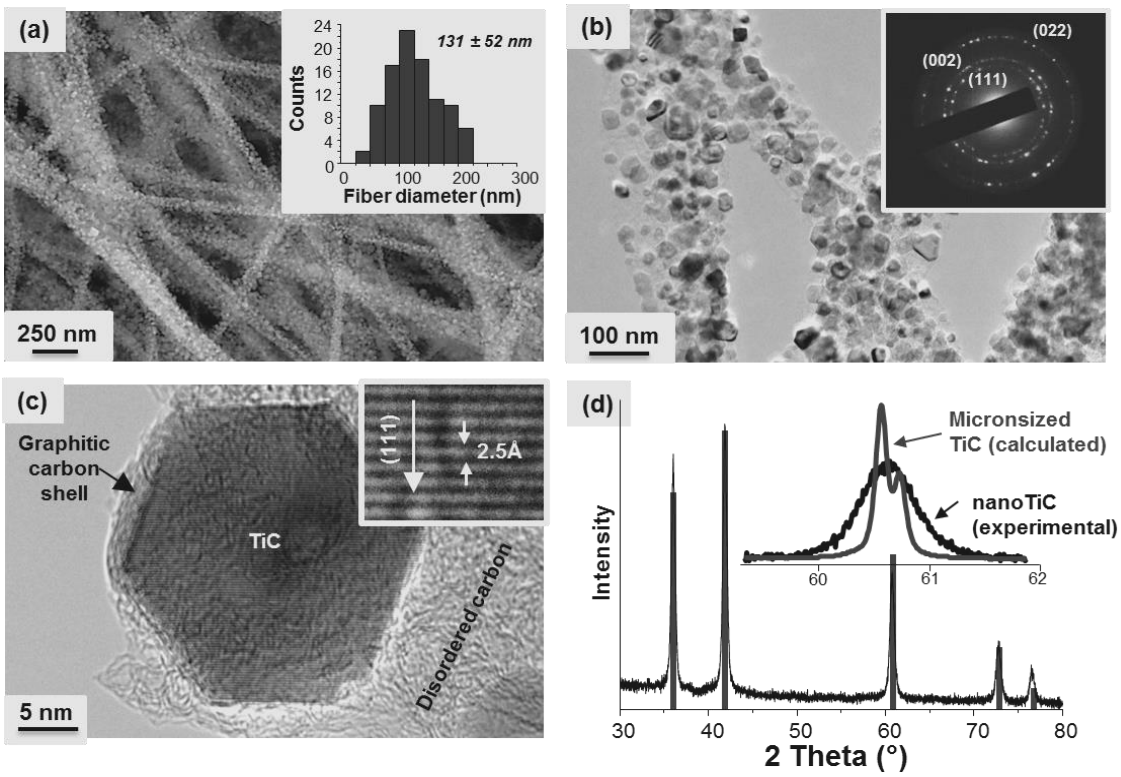

Figure 24. SEM (a) and TEM (b-c) images of electrospun TiC nanofibers (CDC precursor). Each fiber consisted of TiC nanocrystallites. The inset in Fig. 24b shows the electron diffraction pattern along the (111)-, (200)-, and (220)-planes of cubic TiC crystal with d-values of 2.50, 2.19 and 1.55 Å, respectively. The lattice fringes of (111)-planes of a TiC nanocrystallite are shown in the inset of Fig. 24c. The finite size of TiC nanocrystallites resulted in broadening of XRD peaks (d), as compared to the peaks of micron-sized TiC crystals (inset in Fig. 24d; X-axis was stretched by a factor of 12 for better visibility).

After chlorination, the morphology (i.e., size and shape) of the resulting TiC-CDC nano-felts was retained. As depicted in the insets of Fig. 25, the TiC-CDC nano-

felts could be bent without breaking within the linear elastic range, and a maximum bending angle of 30° was observed for both nano-felts (corresponding to the strain of 0.01 for 200 μm-thin felt). Based upon gravimetry, the effective density of 0.14 g/cm^3 was measured for the TiC-CDC nano-felts, which corresponded to a porosity of 94 vol.% comprising the micro- and meso-porosities, and inter-fiber space. The TEM images (Fig. 25a-b) showed the brittle failure of CDC fibers that occurred when the ultimate strain was exceeded.

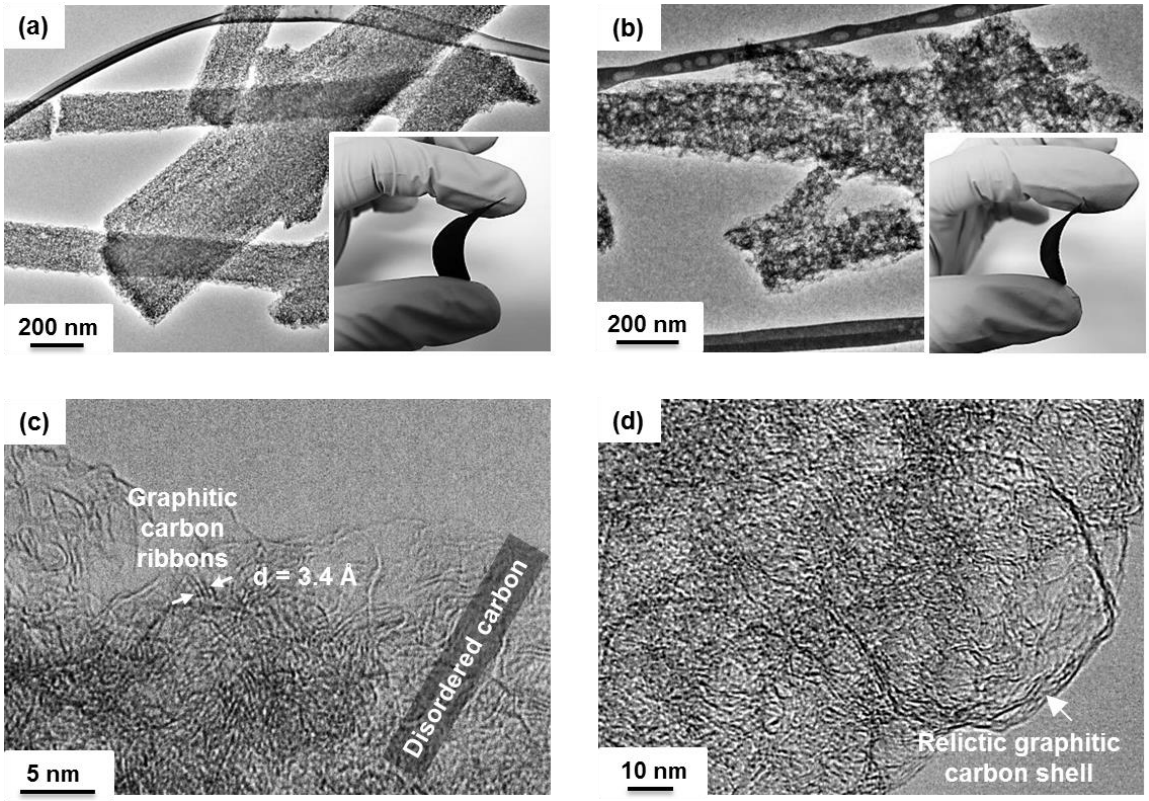

Figure 25. TEM images of the TiC-CDC nano-felts after chlorination at 400 °C (a, c) and 600 °C (b, d). In addition to newly formed CDC, graphitic carbon could be identified in the interface regions of previous TiC nanocrystallites (d). The insets in Fig. 25(a) and (b) demonstrate the flexibility of the developed TiC-CDC nano-felts.

The structural compositions before and after chlorination were investigated by XRD and Raman spectroscopy. With the selected chlorination conditions (6 hrs at 400 or 600 °C), no residual carbide was identified in the resulting TiC-CDC nano-felts (Fig. 26a); two Bragg reflections centered at the 2θ angles of 24° and 44° were attributed to the (002) and (101) crystallographic planes of graphite. The reflections had large values of full-width at half maximum (FWHM), which were characteristic for disordered carbon. Raman spectra of TiC-CDC nano-felts and their electrospun TiC precursor are shown in Fig. 26b. The two bands correlate with in-plane modes including (1) the D-mode at 1342-1353 cm^{-1} that is characteristic for disorder carbon with finite sizes of crystallites, and (2) the graphite G-mode at 1590-1601 cm^{-1} (Table 6). A shoulder at the high-wavenumber part of the G-mode can be

assigned to the D'-mode that indicates the interlayer disorder of graphitic carbon. With the predominant TiC phase having very weak Raman spectrum, only the D- and G-modes of graphitic and disordered carbon were visible in the spectrum of the precursor. The TiC-CDC nano-felt made from chlorination at 400 °C had a larger value of I_D/I_G ratio (i.e., a higher amount of disordered carbon). The reason is that TiC nanocrystallites in the precursor were converted into disordered micro-porous carbon in the resulting CDC nano-felt. With the increase of the chlorination temperature to 600°C, the amount of graphitic carbon increased and the I_D/I_G ratio decreased.

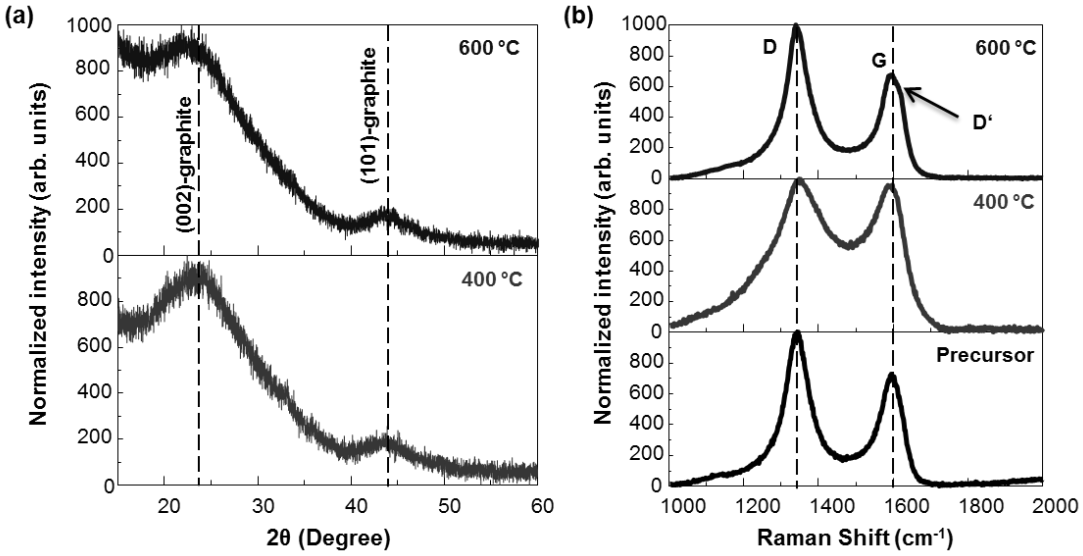

Figure 26. XRD pattern (a) and Raman spectra (b) of TiC-CDC nano-felts and their precursor of electrospun TiC nano-fibrous felt.

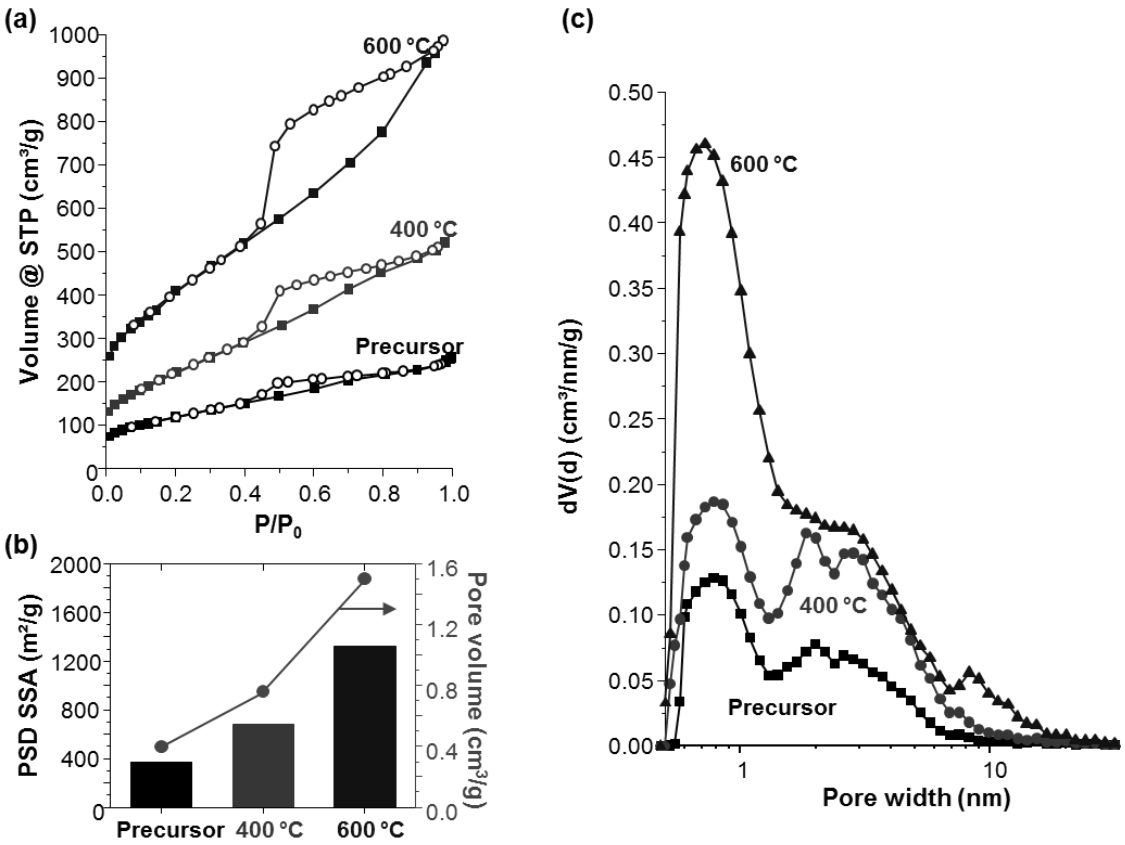

Figure 27. Nitrogen sorption isotherms of TiC-CDC nano-felts and their electrospun TiC precursor (a) indicating the presence of micro- and meso-porous carbons. Compared to those of the precursor, the values of SSA and pore volume were increased as a function of chlorination temperature (b) which is also reflected by the PSD (c).

Table 6. Band position, FWHM, and I_D/I_G ratio from Raman spectra of TiC-CDC nano-felts and their electrospun precursor.

	D-mode (cm^{-1})		G-mode (cm^{-1})		Ratio
	Position	FWHM	Position	FWHM	I_D/I_G
Nano-felt (600 °C)	1343.0	88.1	1593.8	68.6	1.52
Nano-felt (400 °C)	1353.0	186.6	1600.6	66.3	1.64
Precursor	1341.7	80.2	1592.7	80.4	1.43

Gas sorption (employing N_2 and CO_2 as adsorbates) was used to characterize the PSD, SSA, and pore volume of TiC-CDC nano-felts and precursor (Fig. 27a, Table 7). The precursor showed the SSA value of 371 m^2/g, the average pore size of 1.1 nm, and the pore volume of 0.4 cm^3/g. After chlorination at 400 °C, the average

pore size increased to 1.5 nm; with increase of chlorination temperature to from 400 to 600 °C, the SSA value increased from 738 to 1390 m^2/g, and the value of total pore volume increased from 0.76 to 1.50 cm^3/g (Fig. 39b). With a large contribution of sub-nanometer pores from CDC, the average pore size after chlorination at 600 °C was 0.9 nm (Fig. 27c). The combination of nano-scaled pores, partially graphitic carbon (which is electrically conductive), and continuous fibers is attractive particularly for the application of supercapacitor electrode with high power handling capability which will be discussed in more detail in the next section.

Table 7. Values of SSA, PSD, and pore volume acquired from N_2 and CO_2 gas sorption for TiC-CDC nano-felts and the precursor.

	BET SSA (m^2/g)	**PSD SSA (m^2/g)**	**Total pore volume (cm^3/g)**	**Volume of pores < 1.5 nm (cm^3/g)**	**Average pore size (nm)**
Nano-felt (600 °C)	1390	1319	1.50	0.27	0.9
Nano-felt (400 °C)	738	696	0.76	0.14	1.5
Precursor	414	371	0.40	0.09	1.1

Electrochemical Performance

The TiC-CDC nano-felt made from chlorination at 600 °C had an excellent performance of high frequency power handling while having a moderate volumetric capacitance in 1 M H_2SO_4 using a MCE (Fig. 28). Fig. 5a-c shows the CVs (at 1 V/s) of TiC-CDC nano-felts (Fig. 28a), conventional TiC-CDC powder synthesized at 600 °C (Fig. 28b), and carbon onions obtained from annealing of nano-diamonds at 1600 °C (Fig. 28c). It is evident that TiC-CDC nano-felts and carbon onions still show pronounced capacitive behavior at high scan rates whereas the (conventional) TiC-CDC powder behaves dominantly resistive behavior. At a sweep rate of 10 mV/s, the TiC-CDC nano-felt yielded the capacitance of 12 F/cm^3 that dropped to 50 % of the initial value at ~5 V/s and to 30 % with extremely high rate of 100 V/s (Fig. 28d). Conventional, micron-sized TiC-CDC powder (Fig. 40d) and activated carbon fibers (ACFs) lose the capacitance quickly at a moderate scan rate of 100 mV/s; thus, the maximum charge/discharge rates are substantially limited. Bleda-Martinez et al. reported the decrease of capacitance to below 5 % of the initial value at the sweep rate of 100 mV/s for ACF in 1 M Na_2SO_4. At this scan rate, the TiC-CDC nano-felt tested in the MCE maintained 62 % volumetric capacitance of the initial value. A similar superior high frequency behavior was identified for onion-like carbon with high electrical conductivity,[20] but the total capacitance was much lower due to smaller SSA (~500 m^2/g). The moderate volumetric capacitance of the TiC-CDC nano-felt resulted from relatively low packing density of nanofibers inside the cavity of MCE.

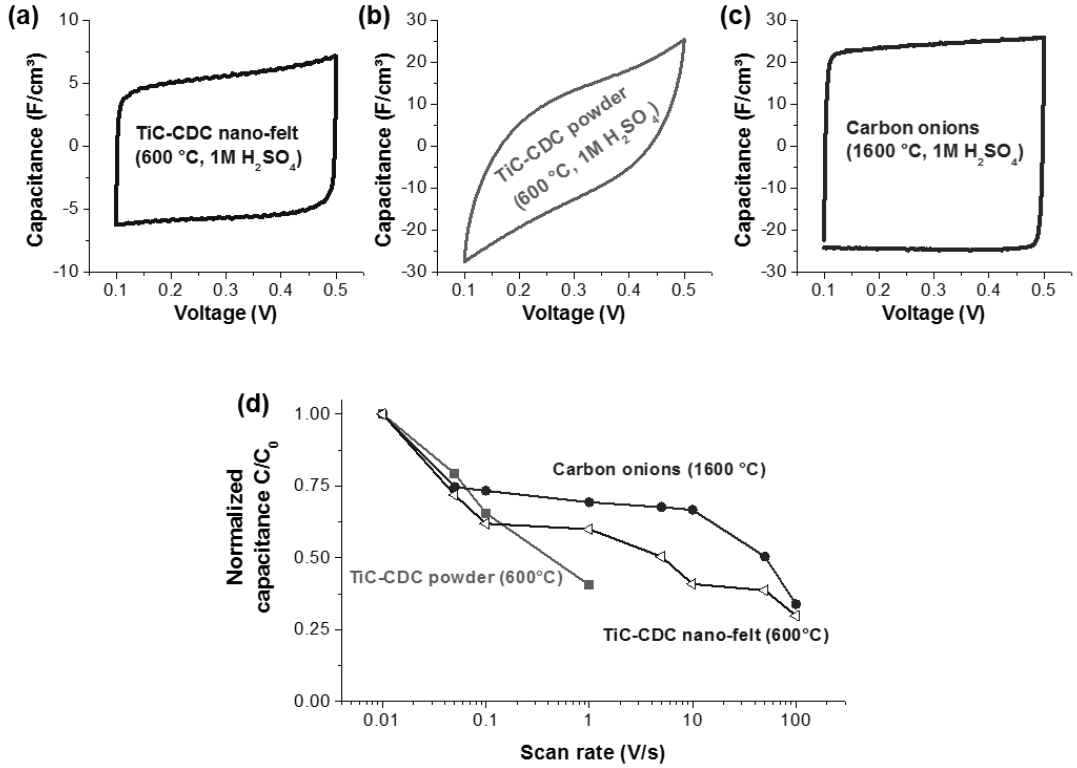

Figure 28. Cyclic voltammograms of the TiC-CDC nano-felt (a) compared to carbon onions (b) and conventional, micron-sized TiC-CDC powder (c) tested in the MCE at 1 V/s in 1 M H_2SO_4 solution. The power-handling ability of TiC-CDC nano-felt was revealed when plotting the scan rate vs. the normalized capacitance C/C_0 (d).

To determine the gravimetric capacitance, the TiC-CDC nano-felts (600 °C) were also tested in a binder-free setup with two symmetrical electrodes in 1 M H_2SO_4 and 1.5 M TEA-BF_4 with galvanostatic charge/discharge and cyclic voltammetry. At a slow scan rate of 10 mV/s, a gravimetric capacitance of 110 F/g and 63 F/g was measured in aqueous and organic electrolytes, respectively. For comparison, TiC-CDC powder electrodes (600 °C synthesis temperature) with 5 wt.% PTFE binder show a gravimetric capacitance of 108 F/g and 140 F/g in 1 M H_2SO_4 and 1.5 M TEA-BF_4, respectively.

As seen from Fig. 29, an increase in the measured current at the edges of 1 V voltage window arises from minor Faradic reactions in 1 M H_2SO_4. A comparable capacitive behavior can also be identified for the nano-felt precursor tested under the same conditions yielding a gravimetric capacitance of 37 F/g. This value is comparable to the capacitance of ACF (43 F/g)[24] and can be explained by the large amount of porous carbon already present in the precursor. The Ohmic resistance (at 100 mA/cm^2) of the nano-felt precursor is 1.4 Ω·cm^2 and increases after chlorination at 400 °C to 2.6 Ω·cm^2 because of the replacement of well-conductive TiC by highly disordered carbon; this is in agreement with the PSD (Fig. 27c) and Raman data (Fig. 26b). CDC nano-felt obtained from synthesis at 600°C had a low

resistance of 0.6 $\Omega \cdot cm^2$ which is in agreement with the observed high power handling ability.

The different gravimetric capacitances obtained from galvanostatic charge-discharge (GC) measurements in organic and aqueous electrolytes at different currents are shown in Fig. 29c. At a low current density of 4 mA/cm^2, a gravimetric capacitance of 102 F/g (1 M H_2SO_4) and 64 F/g (1.5 M TEA-BF_4) was measured. The lower chlorination temperature at 400 °C yielded a lower gravimetric capacitance of the CDC nano-felt of 60 F/g in aqueous electrolytes (10 mV/s). Considering the low specific weight of the material (2.4 mg/cm^2), the current per gram during galvanostatic charge/discharge is much higher than for conventional TiC-CDC films (~15 mg/cm^2). The calculated capacitance values are well in agreement with the results obtained from cyclic voltammetry. It is important to note that when the film was tested as is, an improved rate handling ability was observed compared to MCE testing (Fig. 29d). At a scan rate of 1 V/s, for example, the gravimetric capacitance dropped to 85 % of the initial value for the nano-felt synthesized at 600 °C, but to 60 % when tested in the MCE. When filling the MCE with the sample material, the fibers in the nano-felt are crushed and the continuous connectivity of the fibers is lost. This is also the case for all powder-based supercapacitors and, as seen from Fig. 41d, results in an inferior power-handling ability. Keeping the films intact ensures superior connectivity and significantly improved rate-capability. It is important to note that because of this, the TiC-CDC nano-felt electrodes show a better rate-capability than carbon onions tested in the MCE with a smaller fade in capacitance for scan rates up to 1 V/s. CDC nano-felts synthesized at 400°C showed an inferior power handling ability with a drop of the capacitance to ~70 % of the initial value at 1 V/s because of the lower degree of graphitization.

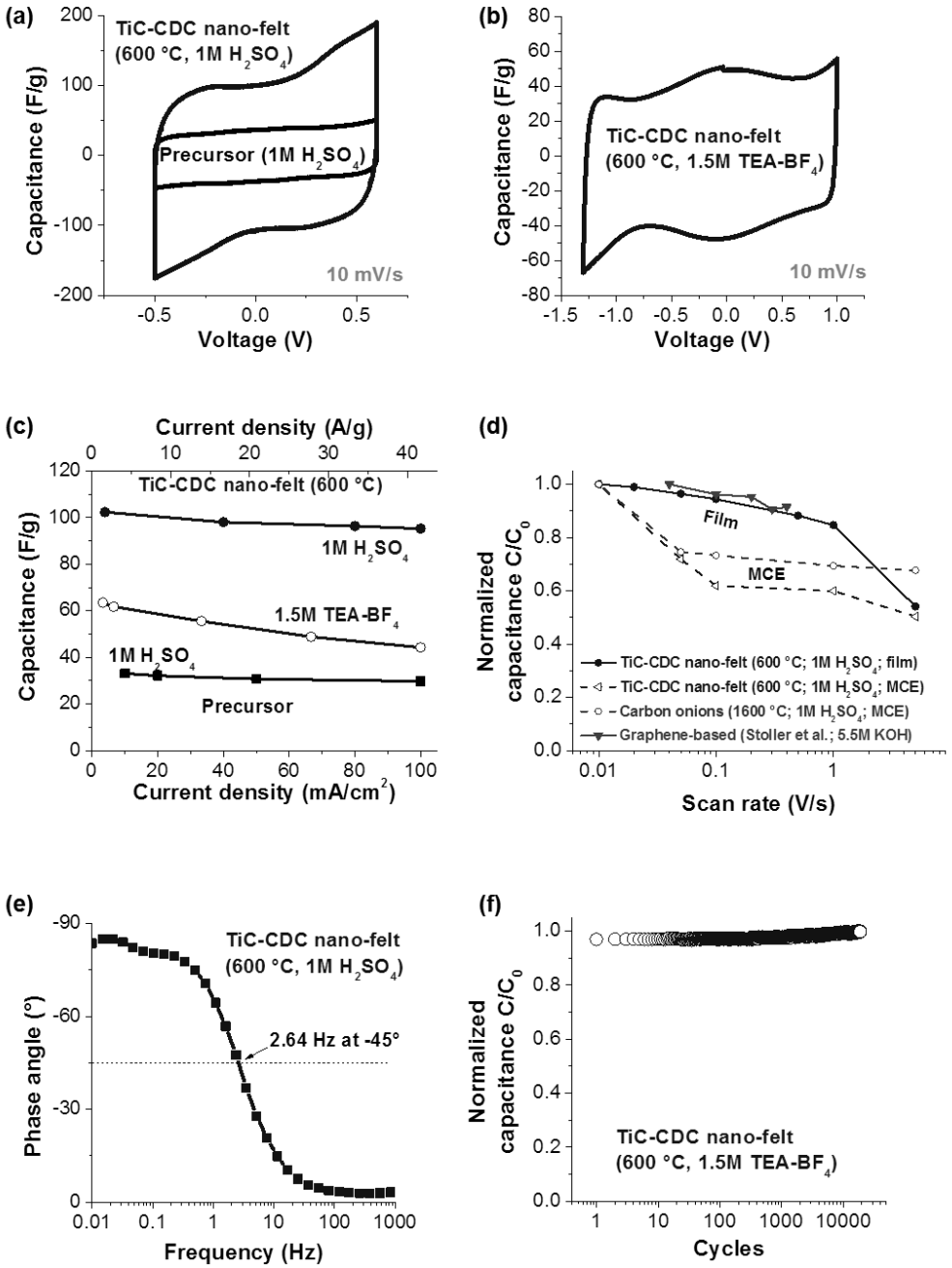

Figure 29. Cyclic voltammograms (CVs, obtained at 10 mV/s for a symmetrical cell setup) of TiC-CDC nano-felt and the precursor in 1 M H_2SO_4 (a) for a 1 V voltage window. CV of the TiC-CDC nano-felt in 1.5 M TEA-BF_4 over an extended voltage window of 2.3 V (b). Gravimetric capacitance obtained via Gravimetric charge/discharge measurements for the TiC-CDC nano-felt in organic and aqueous electrolytes in comparison with the precursor (c) for different current densities. Comparison between the fade in normalized capacitance for the TiC-CDC nano-felt tested as a film (5x5 mm^2) and in the MCE (d). Also included is data for carbon onions tested in the MCE and data reported by Stoller *et al.* [25] for a graphene-based

supercapacitor. Frequency dispersion of the phase angle (e). Cycling stability at 100 mA galvanostatic charge / discharge (f).

With a comparable capacitance in aqueous electrolytes, TiC-CDC nano-felts show a power-handling comparable to graphene-based supercapacitors (Fig. 29d). The only report of a better high-power handling was reported by Pech et al. for electro-deposited onion-like carbon based micro-supercapacitors (30 % of the initial capacitance at 200 V/s); carbon onions, however, have only a modest gravimetric capacitance (≤ 40 F/g).

Fig. 29e shows the dependence of the phase angle with the frequency. For frequencies up to 1 Hz, the phase angle is very close to -90°, which indicates function close to being an ideal capacitor. The characteristic frequency f_0 for a phase angle of -45° is 2.64 Hz. This frequency marks the point at which the resistive and capacitive impedances are equal. The corresponding time constant τ_0 (= $1/f_0$) equals 379 ms compared to 200 s for conventional TiC-CDC synthesized at 600 °C, 1.1 s for carbon-onion macro-devices, 700 ms for MWCNT, and 26 ms for carbon-onion micro-supercapacitors. Also, it is important to note that the high capacitance of CDC nano-felts (synthesized at 600°C) does not fade over thousands of cycles (Fig. 29f).

Conclusions

To the best of our knowledge, the TiC-CDC nano-felts have never been developed and their electrochemical properties have never been studied. Nonetheless, the electrodes made of electrospun nanofibers have been explored before: the supercapacitor electrodes made of electrospun nanofibers of polyamic acid (PAA) or polybenzimidazol (PBI) yielded (in aqueous electrolyte of KOH) high gravimetric capacitance of up to ~180 F/g after activation. In agreement with those studies, the TiC-CDC nano-felts showed a small decrease in gravimetric capacitance at high current densities and only a fade in gravimetric capacitance of 24 % at 12.5 A/g. With the combination of superior electrochemical properties and mechanical flexibility/stability, the TiC-CDC nano-felts are likely to have important applications for the development of high-performance supercapacitors and/or electrodes.

In summary, we demonstrated that the mechanically flexible TiC-CDC nano-felts with superior electrochemical properties were developed through chlorination of electrospun TiC nano-fibrous felts. The TiC-CDC nano-felts retained the morphological properties of the precursor, while had substantially higher values of SSA and pore volume. The developed TiC-CDC nano-felts demonstrated excellent high-power performance when used as an electrode material for electrochemical capacitors. The results of electrochemical characterization in aqueous and organic electrolytes showed that the nano-felts retained 50 % and 30 % of their capacitance at the enormous scan rates of 5 V/s and 100 V/s, respectively. This is a much lower decrease in capacitance as compared to the activated carbon or conventional TiC-CDC powder or bulk electrodes, which are considered to be the best materials for supercapacitor electrodes. The rates above 1 V/s have only been achieved for nanotubes, carbon onions, and graphene, but those have a lower capacitance when

compared to the TiC-CDC nano-felts. This is due to the microstructure of the TiC-CDC nano-felts; *i.e.,* the disordered and extremely porous carbon coexists with graphitic carbon ribbons in the nanofiber network. The structural integrity and resilience of the developed TiC-CDC nano-felts would make them suitable for energy-related applications, particularly the binder-free and flexible supercapacitors and/or electrodes.

Publications:

1. A. Sathe, M.A. Peck, C. Balasanthiran, M.A. Langell, R.M. Rioux, J.D. Hoefelmeyer 'X-ray photoelectron spectroscopy of transition metal ions attached to the surface of rod-shape anatase TiO2 nanocrystals' Inorg. Chim. Acta 2014. DOI: 10.1016/j.ica.2014.08.011

2. C. Balasanthiran, J.D. Hoefelmeyer 'Facile method to attach transition metal ions to the surface of anatase TiO2 nanorods' Chem. Comm. 2014, 50, 5721-5724. DOI: 10.1039/C3CC48945K

3. I.D. Vukoje, E.S. Dzunuzovic, V.V. Vodnik, S. Dmitirijevic, S.P. Ahrenkiel, J.M. Nedeljkovic 'Synthesis, characterization, and antimicrobial activity of poly(GMA-co-EGDMA) polymer decorated with silver nanoparticles' J. Mater. Sci. 2014, 49, 6838-6844. DOI: 10.1007/s10853-014-8386-x

4. U. Bogdanovic, V.V. Vodnik, S.P. Ahrenkiel, M. Stoiljkovic, G. Ciric-Marjanovic, J.M. Nedeljkovic 'Interfacial synthesis and characterization of gold/polyaniline nanocomposites' Synth. Met. 2014, 195, 122-131. DOI: 10.1016/j.synthmet.2014.05.018

5. I. Vukoje, V. Lazic, V.V. Vodnik, M. Mitric, B. Jokic, S.P. Ahrenkiel, J.M. Nedeljkovic, M. Radetic 'The influence of triangular silver nanoplates on antimicrobial activity and color of cotton fabrics pretreated with chitosan' J. Mater. Sci., 2014, 49, 4453-4460. DOI: 10.1007/s10853-014-8142-2

6. C.L. Lai, P. Kolla, Y. Zhao, H. Fong, A.L. Smirnova 'Lignin-derived electrospun carbon nanofiber mats with supercritically deposited Ag nanoparticles for oxygen reduction reaction in alkaline fuel cells' Electrochim. Acta 2014, 130, 431-438. DOI: 10.1016/j.electacta.2014.03.006

7. S. Rasalingam, H.S. Kibombo, C.M. Wu, R. Peng, J. Baltrusaitis, R.T. Koodali 'Competitive role of structural properties of titania-silica mixed oxides and a mechanistic study of the photocatalytic degradation of phenol' Appl. Catal. B 2014, 148, 394-405. DOI: 10.1016/j.apcatb.2013.11.025

8. L. Mahoney, R.T. Koodali ‘Versatility of Evaporation-Induced Self-Assembly (EISA) Method for Preparation of Mesoporous TiO2 for Energy and Environmental Applications’ Materials 2014, 7, 2697-2746. DOI: 10.3390/ma7042697

9. M. Xi, X.X. Wang, Y. Zhao, Q. Feng, F. Zheng, Z.T. Zhu, H. Fong ‘Mechanically flexible hybrid mat consisting of TiO2 and SiO2 nanofibers electrospun via dual spinnerets for photo-detector’ Mater. Lett. 2014, 120, 219-223. DOI: 10.1016/j.matlet.2014.01.110

10. C.L. Lai, Z.P. Zhou, L.F. Zhang, X.X. Wang, Q.X. Zhou, Y. Zhao, C.Y. Wang, X.F. Wu, Z.T. Zhu, H. Fong ‘Free-standing and mechanically flexible mats consisting of electrospun carbon nanofibers made from a natural product of alkali lignin as binder-free electrodes for high-performance supercapacitors’ J. Power. Sources 2014, 247, 134-141. DOI: 10.1016/j.jpowsour.2013.08.082

11. S. Rasalingam, R. Peng, R.T. Koodali ‘Removal of Hazardous Pollutants from Wastewaters: Applications of TiO2-SiO2 Mixed Oxide Materials’ J. Nanomat. 2014, Article No. 617405. DOI: 10.1155/2014/617405

12. S.R. Tamang, J.H. Son, J.D. Hoefelmeyer ‘Preparation of RHgCl via transmetalation of (8-quinolyl)SnMe3 and redistribution to R2Hg (R=8-quinolyl): a highly distorted diorganomercury(II) with 84 degree C-Hg-C angle’ Dalton Trans. 2014, 43, 7139-7145. DOI: 10.1039/c4dt00384e

13. S. Rasalingam, R. Peng, R.T. Koodali ‘An investigation into the effect of porosities on the adsorption of rhodamine B using titania-silica mixed oxide xerogels’ J. Envir. Mgmt. 2013, 128, 530-539. DOI: 10.1016/j.jenvman.2013.06.014

14. H.S. Kibombo, S. Rasalingam, R.T. Koodali ‘Facile template free method for textural property modulation that enhances adsorption and photocatalytic activity of aperiodic titania supported silica materials’ Appl. Catal. B 2013, 142, 119-128. DOI: 10.1016/j.apcatb.2013.05.020

15. H.S. Kibombo, A.S. Weber, C.M. Wu, K.R. Raghupathi, R.T. Koodali ‘Effectively dispersed europium oxide dopants in TiO2 aerogel supports for enhanced photocatalytic pollutant degradation’ J. Photochem. Photobiol. A 2013, 269, 49-58. DOI: 10.1016/j.jphotochem.2013.07.006

16. G.F. He, X.X. Wang, M. Xi, F. Zheng, Z.T. Zhu, H. Fong ‘Fabrication and evaluation of dye-sensitized solar cells with photoanodes based on electrospun TiO2 nanotubes’ Mater. Lett. 2013, 106, 115-118. DOI: 10.1016/j.matlet.2013.05.014

17. N.L. Netzer, Z. Tanaka, B. Chen, C.Y. Jiang ‘Tailoring the SERS Enhancement Mechanisms of Silver Nanowire Langmuir-Blodgett Films via Galvanic Replacement Reaction’ J. Phys. Chem. C 2013, 117, 16187-16194. DOI: 10.1021/jp405796b

18. H.S. Kibombo, C.M. Wu, R. Peng, J. Baltrusaitis, R.T. Koodali ‘Investigation of the role of platinum oxide for the degradation of phenol under simulated solar irradiation’ Appl. Catal. B 2013, 136, 248-259. DOI: 10.1016/j.apcatb.2013.01.062

19. A.M. Hussein, L. Mahoney, R. Peng, H. Kibombo, C.M. Wu, R.T. Koodali, R. Shende ‘Mesoporous coupled ZnO/TiO2 photocatalyst nanocomposites for hydrogen generation’ J. Renew. Sust. Ener. 2013, 5, Article No. 033118. DOI: 10.1063/1.4808263

20. L. Mahoney, C.M. Wu, H.S. Kibombo, E. Thiruppathi, J. Baltrusaitis, S. Rasalingam, R.T. Koodali ‘Exploration of the role of anions in the synthesis of Cr containing mesoporous materials at room temperature’ Microporous Mesoporous Mater. 2013, 170, 211-225. DOI: 10.1016/j.micromeso.2012.12.001

21. Y. Zhao, A. Thapa, Q. Feng, M. Xi, Q.Q. Qiao, H. Fong ‘Electrospun TiC/C nano-felt surface-decorated with Pt nanoparticles as highly efficient and cost-effective counter electrode for dye-sensitized solar cells’ Nanoscale 2013, 5, 11742-11747. DOI: 10.1039/c3nr04170k

22. C. Qiu, Y. Bao, N.L. Netzer, C.Y. Jiang ‘Structure evolution and SERS activation of cuprous oxide microcrystals via chemical etching’ J. Mater. Chem. A 2013, 1, 8790-8797. DOI: 10.1039/c3ta11395g

23. W. Kang, C.S. Spanjers, R.M. Rioux, J.D. Hoefelmeyer ‘Synthesis of brookite TiO2 nanorods with isolated Co(II) surface sites and photocatalytic degradation of 5,8-dihydroxy-1,4-naphthoquinone dye’ J. Mater. Chem. A 2013, 1, 7717-7728. DOI: 10.1039/c3ta11038a

24. H.J. Liu, F. Wang, Y. Zhao, H. Fong ‘Mechanically resilient electrospun TiC nanofibrous mats surface-decorated with Pt nanoparticles for oxygen reduction reaction with enhanced electrocatalytic activities’ Nanoscale 2013, 5, 3643-3647. DOI: 10.1039/c3nr34123b

25. R. Peng, C.M. Wu, J. Baltrusaitis, N.M. Dimitrijevic, T. Rajh, R.T. Koodali ‘Ultra-stable CdS incorporated Ti-MCM-48 mesoporous materials for efficient photocatalytic decomposition of water under visible light illumination’ Chem. Comm. 2013, 49, 3221-3223. DOI: 10.1039/c3cc41362d

26. R. Peng, S. Banerjee, G. Sereda, R.T. Koodali ‘TiO2-SiO2 mixed oxides: Organic ligand templated controlled deposition of titania and their photocatalytic

activities for hydrogen production' Int. J. Hydrog. Ener. 2012, 37, 17009-17018. DOI: 10.1016/j.ijhydene.2012.07.047

27. G. Sereda, C. Marshall, J.A. Libera, J. Dreessen, A. Grady, M. Turner 'Effect of Atomic Layer Deposition Support Thickness on Structural Properties and Oxidative Dehydrogenation of Propane on Alumina- and Titania-Supported Vanadia' Catal. Lett. 2012, 142, 399-407. DOI: 10.1007/s10562-012-0780-x

28. Y. Gao, V. Presser, L.F. Zhang, J.J. Niu, J.K. McDonough, C.R. Perez, H. Lin, H. Fong, Y. Gogotsi 'High power supercapacitor electrodes based on flexible TiC-CDC nano-felts' J. Power. Sources 2012 201, 368-375. DOI: 10.1016/j.jpowsour.2011.10.128

29. L.F. Zhang, X.X. Wang, Y. Zhao, Z.T. Zhu, H. Fong 'Electrospun carbon nano-felt surface-attached with Pd nanoparticles for hydrogen sensing application' Mater. Lett. 2012, 68, 133-136. DOI: 10.1016/j.matlet.2011.10.064

30. R. Peng, D. Zhao, N.M. Dimitrijevic, T. Rajh, R.T. Koodali 'Room Temperature Synthesis of Ti-MCM-48 and Ti-MCM-41 Mesoporous Materials and Their Performance on Photocatalytic Splitting of Water' J. Phys. Chem. C 2012, 116, 1605-1613. DOI: 10.1021/jp210448v

31. Z.P. Zhou, X.F. Wu, H. Fong 'Electrospun carbon nanofibers surface-grafted with vapor-grown carbon nanotubes as hierarchical electrodes for supercapacitors' Appl. Phys. Lett. 2012, 100, Article No. 023115. DOI: 10.1063/1.3676193

32. H.S. Kibombo, R. Peng, S. Rasalingam, R.T. Koodali 'Versatility of heterogeneous photocatalysis: synthetic methodologies epitomizing the role of silica support in TiO2 based mixed oxides' Catal. Sci. Tech. 2012, 2, 1737-1766. DOI: 10.1039/c2cy20247f

33. J.H. Son, J.D. Hoefelmeyer '1,2-Nucleophilic addition of 2-(picolyl)organoboranes to nitrile, aldehyde, ketone, and amide' Org. Biomol. Chem. 2012, 10, 6656-6664. DOI: 10.1039/c2ob25518a

34. A.S. Weber, A.M. Grady, R.T. Koodali 'Lanthanide modified semiconductor photocatalysts' Catal. Sci. Tech. 2012, 2, 683-693. DOI: 10.1039/c2cy00552b

35. S. Mishra, S.P. Ahrenkiel 'Synthesis and Characterization of Electrospun Nanocomposite TiO2 Nanofibers with Ag Nanoparticles for Photocatalysis Applications' J. Nanomat. 2012, Article No. 902491. DOI: 10.1155/2012/902491

36. H.S. Kibombo, R.T. Koodali ‘Heterogeneous Photocatalytic Remediation of Phenol by Platinized Titania-Silica Mixed Oxides under Solar-Simulated Conditions’ J. Phys. Chem. C 2011, 115, 25568-25579. DOI: 10.1021/jp209620j

37. T. Xu, M. Yan, J.D. Hoefelmeyer, Q. Qiao 'Exciton migration and charge transfer in chemically linked P3HT-TiO2 nanorod composite' RSC Advances 2012, DOI: 10.1039/C1RA00739D

38. S. Banerjee, H. Khatri, V. Balasanthiran, R.T. Koodali, G. Sereda 'Synthesis of substituted acetylenes, aryl-alkyl ethers, 2-alkene-4-ynoates and nitriles using heterogeneous mesoporous Pd-MCM-48 as reusable catalyst' Tetrahedron 2011, 67(32), 5717-5724. DOI: 10.1016/j.tet.2011.05.132

39. G. Sereda, T. Kim, A. Jones, H. Khatri, C. Marshall, H. Subramanian, R.T. Koodali, 'Phthalocyanine- and Calixarene-Templating Effect on the Catalytic performance of Solid Supported Vanadates', Catal. Lett., 2011, 141(8), 1086-1096. DOI 10.1007/s10562-011-0662-7

40. G. Sereda, A. Horn, V. Rajpara, R.T. Koodali, M. Urness, A. Kruse, M. Stewart, J. Schloss, A. Rodriguez, M. Amundson, A. Stegmair, A. Zimmerman, R. Woodring, K. McInerney, ‘Benzylic Photooxidation Catalyzed by Carbon-Supported Iron Oxides’, J. Und. Chem. Res., 2011, 10 (2), 118-121.

41. G. Sereda, V. Rajpara, ‘Selective and Clean Cyclohexene-Promoted Oxidation and Photooxidation by Air’, Green and Sustain. Chem., 2011, 1, 26-30.

42. J. Becker, K.R. Raghupathi, J. St. Pierre, D. Zhao, R.T. Koodali, ‘Tuning of the crystallite and particle sizes of ZnO nanocrystalline materials in solvothermal synthesis and their photocatalytic activity for dye degradation’ J. Phys. Chem. C, 2011, 115, 13844-13850. DOI: 10.1021/jp2038653

43. S. Budhi, H.S. Kibombo, D. Zhao, A. Gonshorowski, R.T. Koodali 'Synthesis of titania-silica xerogels by co-solvent induced gelation at ambient temperature' Mater. Lett. 2011, 65, 2136-2138 DOI: 10.1016/j.matlet.2011.04.054

44. V. Presser, L. Zhang, J.J. Niu, J. McDonough, C. Perez, H. Fong, Y. Gogotsi 'Flexible Nano-felts of Carbide-Derived Carbon with Ultra-high Power Handling Capability' Adv. Ener. Mater. 2011, 1(3), 423-430 DOI: 10.1002/aenm.201100047

45. S. Banerjee, A. Horn, H. Khatri, G. Sereda 'A green one-pot multicomponent synthesis of 4H-pyrans and polysubsituted aniline derivatives of biological, pharmacological, and optical applications using silica nanoparticles as reusable catalyst' Tetra. Lett. 2011, 52(16), 1878-1881. DOI: 10.1016/j.tetlet.2011.02.031

46. H.S. Kibombo, D. Zhao, A. Gonshorowski, S. Budhi, M.D. Koppang, R.T. Koodali 'Cosolvent-Induced Gelation and the Hydrothermal Enhancement of the Crystallinity of Titania-Silica Mixed Oxides for the Photocatalytic Remediation of Organic Pollutants' J. Phys. Chem. C 2011, 115(13), 6126-6135. DOI: 10.1021/jp110988j

47. K.R. Raghupathi, R.T. Koodali, A.C. Manna 'Size-Dependent Bacterial Growth Inhibition and Mechanism of Antibacterial Activity of Zinc Oxide Nanoparticles' Langmuir 2011, 27(7), 4020-4028. DOI: 10.1021/la104825u

48. C. Lai, G. Zhong, Z. Yue, G. Chen, L. Zhang, A. Vakili, Y. Wang, L. Zhu, J. Liu, H. Fong 'Investigation of post-spinning stretching process on morphological, structural, and mechanical properties of electrospun polyacrylonitrile copolymer nanofibers' Polymer 2011, 52(2), 519-528. DOI: 10.1016/j.polymer.2010.11.044

(prior to 2nd payment of funds for DE-FG02-08ER64624)

49. S. Banerjee, V. Balasanthiran, R.T. Koodali, G. Sereda 'Pd-MCM-48: a novel recyclable heterogeneous catalyst for chemo- and regioselective hydrogenation of olefins and coupling reactions' Org. Biomol. Chem. 2010, 8, 4316-4321. DOI: 10.1039/C0OB00183J

50. G. Sereda, V. Rajpara 'Photoactivated and photopassivated benzylic oxidation catalyzed by pristine and oxidized carbons' Catal. Comm. 2011, 12(7), 669-672. DOI: 10.1016/j.catcom.2010.12.027

51. G. Sereda, V. Rajpara 'Exploration of Solid-Supported Reactions with Gold Nanoparticles' J. Chem. Ed. 2010, 87(9), 978-980.

52. D. Zhao, A. Rodriguez, N.M. Dimitrijevic, T. Rajh, R.T. Koodali 'Synthesis, Structural Characterization, and Photocatalytic Performance of Mesoporous W-MCM-48' J. Phys. Chem. C 2010, 114, 15278-15734.

53. L. Zhang, J. Hu, A.A. Voevodin, H. Fong 'Synthesis of Continuous TiC Nanofibers and/or Nanoribbons Through Electrospinning Followed by Carbothermal Reduction' Nanoscale 2010, 2, 1670-1673.

54. J.C. Johnson, S.P. Ahrenkiel, P. Dutta, V.R. Bommisetty 'Nucleation and Growth of Crystalline Grains in RF-Sputtered TiO2 Films' Res. Lett. Nanotech. 2009, 280797.

55. S. Banerjee, G. Sereda 'One-step, Three-component Synthesis of Highly Substituted Pyridines Using Silica Nanoparticles as Reusable Catalyst' Tetra. Lett. 2009, 50(50), 6959-6962.

56. Z.C. Wu, Y. Zhang, T.X. Tao, L. Zhang, H. Fong 'Silver nanoparticles on amidoxime fibers for photo-catalytic degradation of organic dyes in waste water' Appl. Surf. Sci. 2010, 257, 1092-1097.

57. J. Liu, Y. Tian, Y. Chen, J. Liang, L. Zhang, H. Fong 'A surface treatment technique of electrochemical oxidation to simultaneously improve the interfacial bonding strength and the tensile strength of PAN-based carbon fibers' Mater. Chem. Phys. 2010, 122(2-3), 548-555.

58. J. Liu, P. Zhou, L. Zhang, Z. Ma, J. Liang, H. Fong 'Thermo-chemical reactions occurring during the oxidative stabilization of electrospun polyacrylonitrile precursor nanofibers and the resulting structural conversions' Carbon, 2009, 47(4), 1087-1095.

59. D. Zhao, S. Budhi, A. Rodriguez, R.T. Koodali 'Rapid and facile synthesis of Ti-MCM-48 mesoporous material and the photocatalytic performance for hydrogen evolution' Int. J. Hydrogen. Ener. 2010, 35(11), 5276-5283.

60. S. Wen, L. Liu, L. Zhang, Q. Chen, L. Zhang, H. Fong 'Hierarchical electrospun SiO2 nanofibers containing SiO2 nanoparticles with controllable surface-roughness and/or porosity' Mater. Lett. 2010, 64(13), 1517-1520.

61. Z. Zhou, K. Liu, C. Lai, L. Zhang, J. Li, H. Hou, D.H. Reneker, H. Fong 'Graphitic carbon nanofibers developed from bundles of aligned electrospun polyacrylonitrile nanofibers containing phosphoric acid' Polymer, 2010, 51(11), 2360-2367.

62. Z. Zhou, C. Lai, L. Zhang, Y. Qian, H. Hou, D.H. Reneker, H. Fong 'Development of carbon nanofibers from aligned electrospun polyacrylonitrile nanofiber bundles and characterization of their microstructural, electrical, and mechanical properties' Polymer 2009, 50(13), 2999-3006.

63. J. H. Son, M.A. Pudenz, J.D. Hoefelmeyer 'Reactivity of the Bifunctional Ambiphilic Molecule 8-(dimesitylboryl)quinoline: Hydrolysis and Coordination to CuI, AgI and PdII' Dalton Trans. 2010, DOI: 10.1039/C0DT00798F.

64. R.T. Koodali, D. Zhao 'Photocatalytic degradation of aqueous organic pollutants using titania supported periodic mesoporous silica' Energy Environ. Sci. 2010, 3, 608-614.

65. V. Rajpara, S. Banerjee, G. Sereda 'Iron Oxide Nanoparticles Grown on Carboxy-Functionalized Graphite: An Efficient Reusable Catalyst for Alkylation of Arenes' Synthesis, 2010, 16, 2835-2840. DOI: 10.1055/s-0029-1218851

66. R. Chandrasekar, J.Y. Howe, L. Zhang, H. Fong 'Fabrication and Characterization of Electrospun Titania Nanofibers' J. Mater. Sci. 2009, 44 (5), 1198-1205.

67. P. Joshi, L. Zhang, D. Davoux, L. Liu, D. Galipeau, H. Fong, Q. Qiao 'Nanofiber/Nanoparticle Composites for Highly Efficient Dye Sensitized Solar Cells', Energy Environ. Sci. 2010, 3, 1507-1510.